JCI insight

Mitochondrial arginase-2 is a cell-autonomous regulator of CD8$^+$ T cell function and antitumor efficacy

Adrià-Arnau Martí i Líndez,[1] Isabelle Dunand-Sauthier,[1] Mark Conti,[1] Florian Gobet,[1] Nicolás Núñez,[2] J. Thomas Hannich,[3] Howard Riezman,[3] Roger Geiger,[4] Alessandra Piersigilli,[5,6] Kerstin Hahn,[6] Sylvain Lemeille,[1] Burkhard Becher,[2] Thibaut De Smedt,[1] Stéphanie Hugues,[1] and Walter Reith[1]

[1]Department of Pathology and Immunology, Faculty of Medicine, University of Geneva, Geneva, Switzerland. [2]Institute of Experimental Immunology, University of Zurich, Zurich, Switzerland. [3]Department of Biochemistry, NCCR Chemical Biology, University of Geneva, Geneva, Switzerland. [4]Institute for Research in Biomedicine, Università della Svizzera italiana, Bellinzona, Switzerland. [5]Histology Core Facility, School of Life Sciences, Ecole Polytechnique Fédérale de Lausanne, Lausanne, Switzerland. [6]Institute of Animal Pathology, Vetsuisse Faculty, University of Bern, Bern, Switzerland.

As sufficient extracellular arginine is crucial for T cell function, depletion of extracellular arginine by elevated arginase 1 (Arg1) activity has emerged as a hallmark immunosuppressive mechanism. However, the potential cell-autonomous roles of arginases in T cells have remained unexplored. Here, we show that the arginase isoform expressed by T cells, the mitochondrial Arg2, is a cell-intrinsic regulator of CD8$^+$ T cell activity. Both germline *Arg2* deletion and adoptive transfer of *Arg2*$^{-/-}$ CD8$^+$ T cells significantly reduced tumor growth in preclinical cancer models by enhancing CD8$^+$ T cell activation, effector function, and persistence. Transcriptomic, proteomic, and high-dimensional flow cytometry characterization revealed a CD8$^+$ T cell–intrinsic role of Arg2 in modulating T cell activation, antitumor cytoxicity, and memory formation, independently of extracellular arginine availability. Furthermore, specific deletion of *Arg2* in CD8$^+$ T cells strongly synergized with PD-1 blockade for the control of tumor growth and animal survival. These observations, coupled with the finding that pharmacologic arginase inhibition accelerates activation of ex vivo human T cells, unveil Arg2 as a potentially new therapeutic target for T cell–based cancer immunotherapies.

Introduction

An appropriate supply of extracellular L-arginine, a semiessential amino acid that has long been associated with the amelioration of immune responses (1–5), is essential for T cell function (6). Both human and mouse T cells require sufficient extracellular arginine for expression of the T cell receptor–associated (TCR-associated) CD3ζ chain, cell cycle progression and proliferation, cytokine production, and memory differentiation (7–9). Thus, depletion of extracellular arginine is one of the mechanisms that tumors exploit to create an immunosuppressive microenvironment restraining antitumor T cell responses.

In addition to being an essential building block for protein synthesis, arginine is a substrate for several enzymes, including nitric oxide synthases (NOS) and arginases, the latter converting arginine into urea and ornithine. Mammals have 2 arginases, Arg1 and Arg2, which differ in their intracellular localization, expression patterns, and biological significance. Arg1 is the isoform for which the biological roles have been most well defined. It is a cytosolic enzyme best known for its prominent role in the hepatic urea cycle, and it is critical for ammonia detoxification (10). However, in many cancer types, elevated Arg1 activity from tumor cells or tumor-associated myeloid cells participates in the establishment of an arginine-poor immunosuppressive microenvironment.

Arg2 is a mitochondrial enzyme that has a widespread pattern of expression, present in diverse cell types (10, 11). *Arg2* is attributed to correspond to the ancestral gene from which *Arg1* emerged by duplication during animal terrestrial adaptation (12). There is some evidence that Arg2 can, like Arg1, exert immunosuppressive effects by inducing extracellular arginine depletion. For instance, we previously demonstrated that the miR155 represses Arg2 expression in DCs to ultimately establish an arginine-rich microenvironment, which is permissive for T cell proliferation (13). Similarly, Arg2 expression by fetal

Conflict of interest: The technology transfer office (UNITEC) of the University of Geneva applied for a patent related to the inhibition of ARG2 in immune cells in the context of cancer therapy (WO/2019/145453). AAML, IDS, TDS, and WR are inventors on this patent application.

Copyright: © 2019, American Society for Clinical Investigation.

Submitted: August 28, 2019
Accepted: November 13, 2019
Published: November 21, 2019.

Reference information: *JCI Insight*. 2019;4(24):e132975. https://doi.org/10.1172/jci.insight.132975.

DCs and neonatal erythroid cells was reported to quench deleterious T cell responses (14, 15) during pregnancy and in newborns.

In contrast to the aforementioned mechanisms, invoking immunosuppressive effects of extracellular arginine depletion by arginases, recent evidence has also suggested that Arg2 could have direct cell-autonomous roles in T cells themselves. Pharmacological arginase inhibition was found to increase in vitro survival of human T cells, which express only Arg2 (16). Additionally, enhanced survival was also observed for *Arg2*-deficient mouse T cells (16). Because these experiments were performed under excess arginine conditions, and therefore independent of extracellular arginine availability, they argue for a cell-autonomous role of Arg2. The mitochondrial localization of Arg2 raises the intriguing possibility that such observations could be due to a direct effect of Arg2 on T cell metabolism. However, T cell autonomous roles of Arg2 have not been defined, to date.

Here, we investigated the functional repercussions of genetic ablation of *Arg2* in mouse CD8$^+$ T cells using preclinical cancer models as in vivo readouts for CD8$^+$ T cell responses. Intriguingly, *Arg2*-deficient CD8$^+$ T cells were markedly superior at controlling tumor growth and in a manner exhibiting strong synergy with PD-1 blockade. In vivo and in vitro experiments demonstrated that the potentiated antitumor activity of *Arg2*-deficient CD8$^+$ T cells could be attributed to accelerated activation kinetics, the acquisition of more robust effector functions, increased persistence of the T cell response, and enhanced memory T cell formation. These alterations were due to cell-autonomous mechanisms, as they were observed in an otherwise Arg2-proficient background in vivo or independently of extracellular arginine availability in vitro. Notably, pharmacological arginase inhibition in human CD8$^+$ T cells recapitulated the enhanced activation phenotype observed in mouse *Arg2*$^{-/-}$ CD8$^+$ T cells, suggesting a conserved regulatory function of Arg2 in T cells. Taken together, our results demonstrate a potentially novel cell-autonomous role of Arg2 for the modulation of T cell function. Moreover, they pave the way for the development of novel strategies to enhance the efficacy and persistence of T cell–based cancer immunotherapies by targeting Arg2 expression or function in T cells.

Results

Arg2$^{-/-}$ *mice exhibit enhanced antitumor responses*. To investigate the in vivo relevance of Arg2 in antitumor immune responses, *Arg2*$^{-/-}$ mice (17) were injected s.c. with syngeneic B16 melanoma or MC38 colorectal carcinoma cells expressing OVA as surrogate tumor antigen. Growth of B16-OVA and MC38-OVA tumors was significantly reduced in *Arg2*$^{-/-}$ males and females (Figure 1, A and C, and Supplemental Figure 1, A and B; supplemental material available online with this article; https://doi.org/10.1172/jci.insight.132975DS1), yielding smaller tumors 12 or 14 days after tumor injection, respectively (Figure 1, B and D). Up to 60% of male *Arg2*$^{-/-}$ mice remained tumor free (Supplemental Figure 1B). Major populations of CD4$^+$ and CD8$^+$ tumor-infiltrating lymphocytes (TILs) present within MC38-OVA tumors were quantified by flow cytometry. Tumors in *Arg2*$^{-/-}$ mice presented significantly elevated frequencies of CD8$^+$ TILs, whereas frequencies of total CD4$^+$ TILs remained unchanged (Figure 1, E and F). However, the frequencies of CD4$^+$FoxP3$^+$ Tregs were reduced (Figure 1G) in tumors of *Arg2*$^{-/-}$ hosts; consequently, the CD8$^+$/Treg ratio was 3-fold greater in such tumors (Figure 1H). Moreover, ex vivo restimulation demonstrated that IFN-γ expression in CD4$^+$ TILs was superior in *Arg2*$^{-/-}$ hosts (Supplemental Figure 1C), and a similar tendency was also observed for CD8$^+$ TILs. The latter cells also showed reduced CTLA-4 expression (Figure 1, I and J). All mentioned differences were restricted to T cells in the effector site, as they were not observed for T cells in tumor-draining lymph nodes (TdLNs).

As arginine is an essential nutrient for T cells, we measured arginine levels by high-performance liquid chromatography–mass spectrometry (HPLC-MS) in naive and tumor-bearing mice. As described previously (17), naive *Arg2*$^{-/-}$ mice presented approximately 1.5-fold higher serum arginine concentrations (Figure 1K), indicating a major contribution of Arg2 to the homeostasis of circulating arginine. *Arg2*$^{-/-}$ mice also presented higher concentrations of arginine in secondary lymphoid organs (Figure 1L), suggesting a considerable level of Arg2 activity in these tissues. Furthermore, more elevated arginine concentrations were detected in B16-OVA tumors growing in *Arg2*$^{-/-}$ hosts (Figure 1M), advocating for a more favorable tumor microenvironment (TME) in these hosts with increased arginine availability.

Collectively, these results suggest that systemic Arg2 deficiency leads to reduced tumor growth as a consequence of increased infiltration by CD8$^+$ TILs, which could function more efficiently in a more hospitable TME, with higher arginine availability and reduced immunosuppressive pressure from Tregs.

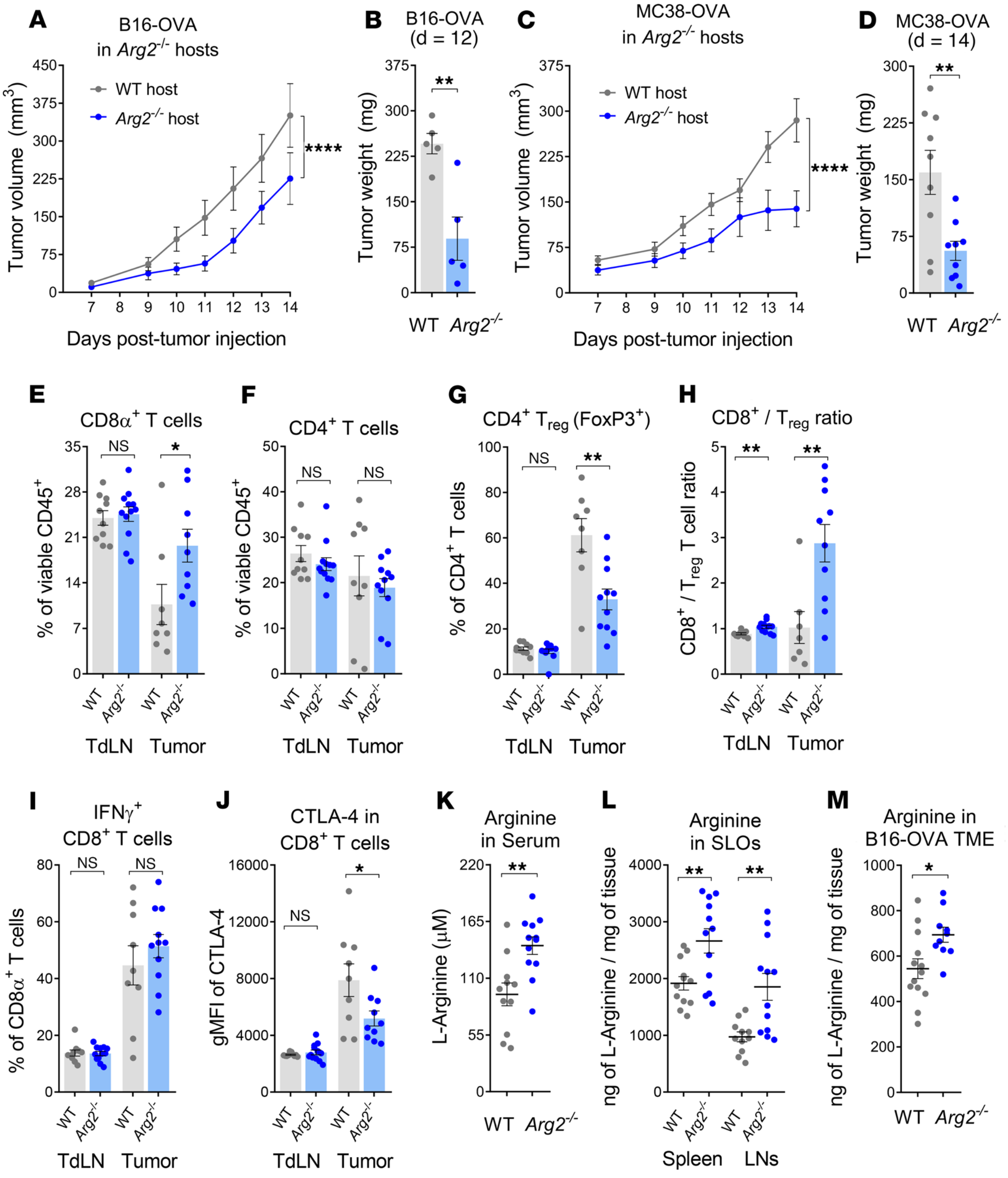

Figure 1. Deletion of *Arg2* reduces tumor growth and increases arginine availability. (**A–D**) Analysis of tumor growth (**A**) for B16-OVA (n = 10) and (**C**) for MC38-OVA (n = 13) and tumor weight at (**B**) day 12 or (**D**) day 14 tumors in WT or *Arg2*$^{-/-}$ hosts. (**E–I**) T cell frequencies in tumor-draining lymph nodes (TdLN) and tumors in 9-day MC38-OVA tumor-bearing WT and *Arg2*$^{-/-}$ mice: (**E**) CD8$^+$ T cells; (**F**) CD4$^+$ T cells; (**G**) FoxP3$^+$ Tregs; (**H**) CD8$^+$/FoxP3$^+$ T cell ratio; (**I**) IFN-γ$^+$CD8$^+$ T cells. (**J**) Analysis of CTLA-4 expression by CD8$^+$ T cells. (**K–M**) HPLC-MS quantification of arginine in (**K**) serum, (**L**) secondary lymphoid organs (SLO), and (**M**) B16-OVA tumors 12 days after tumor implantation in WT or *Arg2*$^{-/-}$ mice. Results were pooled from 2 or 3 independent experiments (**A**, **C**, **E–M**) or are representative of 3 independent experiments (**B** and **D**). Data is represented as mean ± SEM throughout. $^*P < 0.05$, $^{**}P < 0.01$, and $^{****}P < 0.0001$ (**A** and **C**: 2-way ANOVA) (**B**, **D–M**: 2-tailed Student's t test).

To exclude the possibility that enhanced tumor control in *Arg2*$^{-/-}$ mice might be secondary to major genotype-related developmental or anatomical defects, we also performed comprehensive histopathological and flow cytometry analyses. No overt morphological or histological abnormalities were evident in any organs in either young or aged *Arg2*$^{-/-}$ mice (Supplemental Table 1). Young *Arg2*$^{-/-}$ males presented a slight increase in heart weight, and both young and aged *Arg2*$^{-/-}$ males and females exhibited a moderate increase in spleen weight (Supplemental Figure 1, D and E), although no prevalent pathological conditions were associated with these increases in organ weight (Supplemental Table 1, A and B). Additional flow cytometry experiments also demonstrated that frequencies of major DC and

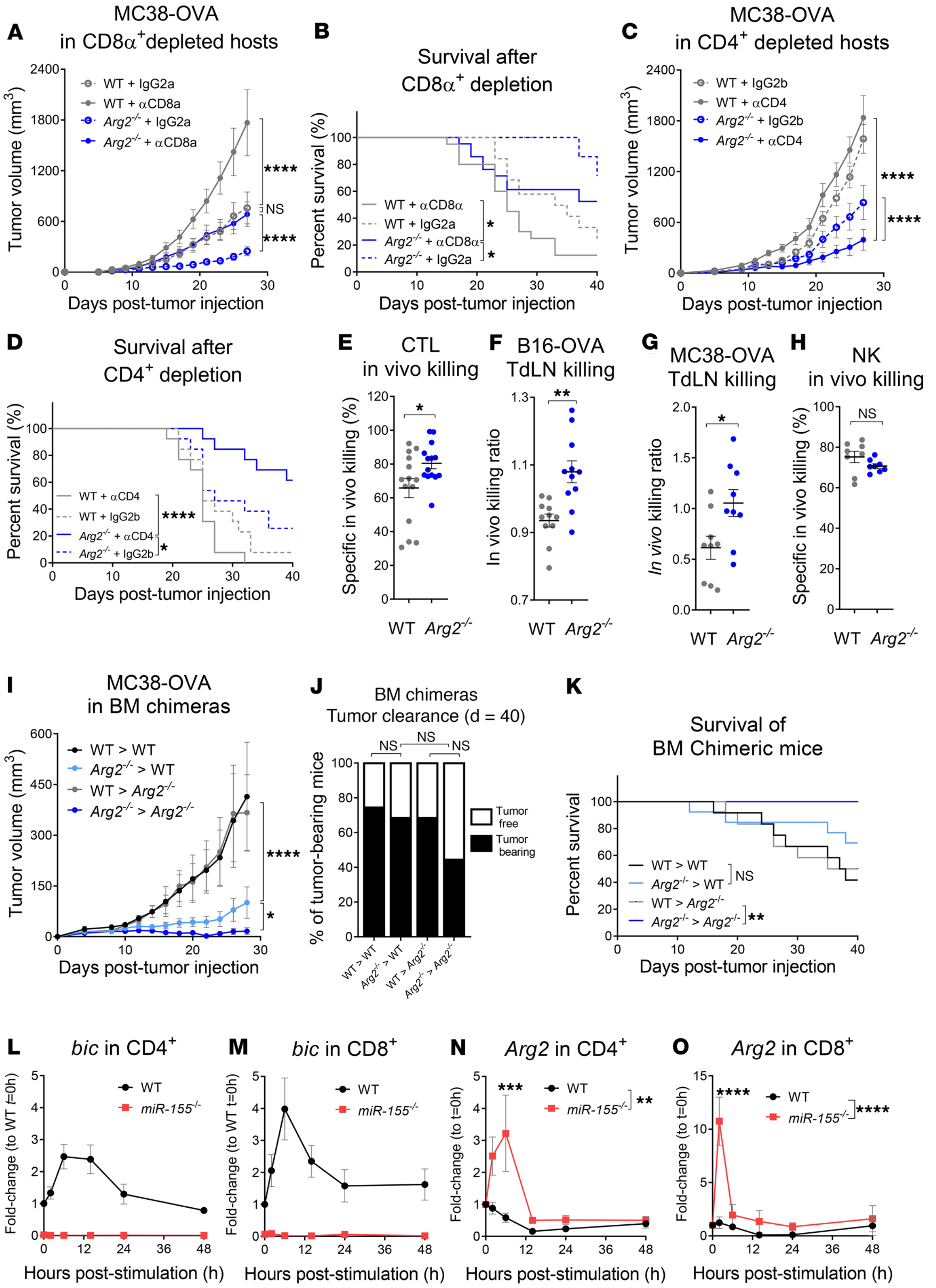

Figure 2. *Arg2*$^{-/-}$ mice control tumor growth more efficiently via enhanced cytotoxic CD8$^+$ T cell function. (**A**) Tumor growth and (**B**) mouse survival in MC38-OVA tumor-bearing WT or *Arg2*$^{-/-}$ mice treated with CD8$^+$ T cell–depleting (αCD8α) or isotype control (IgG2a) antibodies (*n* = 18–21). (**C**) Tumor growth and (**D**) mouse survival were analyzed in MC38-OVA tumor-bearing WT or *Arg2*$^{-/-}$ mice treated with CD4$^+$ T cell depleting (αCD4) or isotype control (IgG2b) antibodies (*n* = 11–12). (**A–D**) Mice received 4 mg/kg doses of depleting or control antibody at days –3, –1, 1, 4, 8, 11, 15, and 18 relative to tumor injection. (**E**) WT and *Arg2*$^{-/-}$ mice that had been immunized 6 days earlier with OVA$_{257-264}$ and CpG-B were implanted with CTV^{lo} control or CTV^{hi} OVA$_{257-264}$–loaded syngeneic splenocytes, and target cell clearance was evaluated in the spleens after 24 hours. (**F** and **G**) CTV^{lo} control or CTV^{hi} OVA$_{257-264}$–loaded syngeneic splenocytes were transferred into 11-day (**F**) B16-OVA or (**G**) MC38-OVA tumor-bearing WT or *Arg2*$^{-/-}$ mice, and target cell clearance was evaluated after 24 hours in the tumor-draining lymph nodes (TdLNs) and contralateral nondraining lymph nodes (ndLNs). Target cell clearance in the TdLNs is expressed as killing ratio relative to the control cells and was normalized relative to the killing ratio in the ndLNs. (**H**) Naive WT or *Arg2*$^{-/-}$ mice received CTV^{lo} control or CTV^{hi}

$\beta 2m^{-/-}$ syngeneic splenocytes, and target cell clearance was evaluated in spleen after 24 hours. Target cell clearance is expressed as killing ratio relative to the control cells. (**I**) Tumor growth, (**J**) tumor clearance rates at day 40, and (**K**) mouse survival were assessed in the indicated 4 groups of BM chimeric mice (n = 11–12). (**L–O**) miR155 (*bic* RNA) or *Arg2* mRNA were quantified by real-time PCR over a 48-hour time course in ex vivo WT or $miR155^{-/-}$ $CD4^+$ (**L** and **N**) or $CD8^+$ (**M** and **O**) T cells activated with αCD3ε and αCD28 antibodies (n = 6). (**A–O**) Results were pooled from 2 or 3 independent experiments. Data is represented as mean ± SEM throughout. *$P < 0.05$, **$P < 0.01$, ***$P < 0.001$, and ****$P < 0.0001$ (**A**, **C**, **I**, **L–O**: 2-way ANOVA) (**E–G**: 2-tailed Student's t test) (**B**, **D**, **K**: log-rank Mantel-Cox test) (**J**: Fisher's exact test).

lymphocyte populations were not altered significantly in the spleens or lymph nodes (LNs) of $Arg2^{-/-}$ mice (Supplemental Figure 1F).

Enhanced antitumor $CD8^+$ T cell responses in $Arg2^{-/-}$ mice. We next performed antibody-mediated depletion experiments to assess the respective roles of $CD4^+$ and $CD8^+$ T cells in the control of tumor growth in WT and $Arg2^{-/-}$ mice. Depletion of $CD8^+$ T cells in $Arg2^{-/-}$ mice impaired their capacity to control tumor growth; tumors grew more aggressively than in isotype-injected $Arg2^{-/-}$ controls and reduced mouse survival (Figure 2, A and B). However, this loss of tumor control did not fully recapitulate what was observed upon depletion of $CD8^+$ T cells in WT hosts, suggesting that additional mechanisms are at play in $Arg2^{-/-}$ hosts. One possible explanation is that residual $CD8^+$ T cells present in the depleted mice (Supplemental Figure 2A) are more effective at controlling tumor growth in the $Arg2^{-/-}$ background because they encounter fewer tumor-infiltrating Tregs (Figure 1H) or because they encounter a more arginine-rich TME (Figure 1M). Depletion of $CD4^+$ T cells markedly improved tumor control and mouse survival in $Arg2^{-/-}$ mice but had little effect in WT mice (Figure 2, C and D). These results indicate that $CD8^+$ T cells confer enhanced protection against tumor growth in both WT and $Arg2^{-/-}$ hosts, whereas $CD4^+$ T cells exert an immunosuppressive effect that is more evident in $Arg2^{-/-}$ hosts.

To confirm that cytotoxic antitumor $CD8^+$ T cell responses are enhanced in $Arg2^{-/-}$ mice, we performed in vivo killing assays. In these experiments, mice that had been preimmunized 6 days earlier with MHC class I–restricted $OVA_{257-264}$ peptide were inoculated with syngeneic $OVA_{257-264}$–loaded and unloaded splenocytes. Twenty-four hours later, we assessed the relative clearance of the 2 splenocyte populations in host spleens by flow cytometry. $Arg2^{-/-}$ hosts showed significantly increased clearance of $OVA_{257-264}$–loaded splenocytes (Figure 2E). A similar approach was used to assess $CD8^+$ T cell cytotoxicity, in a tumor context, in TdLNs of B16-OVA or MC38-OVA tumor-bearing mice. In both tumor models $Arg2^{-/-}$ hosts showed superior clearance of $OVA_{257-264}$–loaded splenocytes (Figure 2, F and G). These results demonstrate that $Arg2^{-/-}$ mice indeed exhibit enhanced $CD8^+$ T cell cytotoxicity.

To determine whether NK cell cytotoxic activity might also be affected by Arg2 deficiency, congenic $B2m^{-/-}$ splenocytes were transferred into naive WT or $Arg2^{-/-}$ mice. In this case, the MHC class I–deficient splenocytes were cleared equally in WT and $Arg2^{-/-}$ hosts (Figure 2H). Thus, in contrast to $CD8^+$ T cell responses, NK cell cytotoxicity is not significantly altered in $Arg2^{-/-}$ mice and cannot account for enhanced tumor control observed in $CD8^+$ T cell–depleted $Arg2^{-/-}$ mice relative to $CD8^+$ T cell–depleted WT mice (Figure 2A).

To investigate whether Arg2 deficiency in radioresistant or BM-derived cells is responsible for enhanced antitumor responses in $Arg2^{-/-}$ mice, we next assessed MC38-OVA tumor growth in BM chimeras. Both WT and $Arg2^{-/-}$ hosts reconstituted with $Arg2^{-/-}$ BM exhibited a strong reduction in tumor growth compared with WT or $Arg2^{-/-}$ hosts reconstituted with WT BM (Figure 2I). Consequently, tumor-bearing chimeras reconstituted with $Arg2^{-/-}$ BM exhibited improved tumor clearance rates and prolonged survival (Figure 2, J and K), firmly suggesting that enhanced tumor control in $Arg2^{-/-}$ mice is therefore mainly due to the loss of Arg2 expression in cells of hematopoietic origin. Additionally, a small but significant difference between $Arg2^{-/-}$-reconstitued WT and $Arg2^{-/-}$ suggests a minor contribution from radioresistant cells for tumor control in $Arg2^{-/-}$ hosts.

Arg2 deficiency improves T cell function in vitro. As mentioned above, we previously reported that inhibition of *Arg2* mRNA expression by miR155 is required for optimal DC function (13). To determine whether this control of Arg2 expression also takes place in T cells, we quantified *Arg2* mRNA by quantitative PCR (qPCR) in WT and miR155-deficient T cells at different times after αCD3ε/αCD28 activation (Figure 2, L–O, and Supplemental Figure 1, G and H). The results demonstrated that induction of miR155 expression (Figure 2, L and M) indeed suppresses an early (prior to 12 hours) and transient increase in *Arg2* mRNA abundance in $CD4^+$ and $CD8^+$ T cells (Figure 2, N and O). Instead, *Arg1* mRNA was barely detectable in activated T cells and not subject to regulation by miR155 (Supplemental Figure 1, G and H). These results suggest that suppression of *Arg2* expression in activated T cells could also be required for their optimal function.

To investigate the functional impact of suppressing Arg2 expression in T cells, we searched for phenotypic changes between WT and $Arg2^{-/-}$ OT-I $CD8^+$ T cells activated in vitro with anti-CD3ε and anti-CD28 antibodies.

Flow cytometry experiments indicated that *Arg2*$^{-/-}$ cells exhibited faster and stronger activation dynamics: shedding of CD62L occurred significantly faster in *Arg2*$^{-/-}$ cells, becoming already evident within the first hour of activation (Figure 3, A and B); upregulation of CD69 was higher in *Arg2*$^{-/-}$ cells and remained more robustly higher, even after arginine concentrations in the culture medium were reduced to limiting levels (Figure 3C). In contrast, CellTrace Violet (CTV) dilution assays revealed that the proliferative capacity of *Arg2*$^{-/-}$ cells was not affected at any of the tested arginine concentrations (Supplemental Figure 3, A and B).

Notably, pharmacologic inhibition of ARG2 also increased the activation dynamics of ex vivo–cultured human T cells. Thus, 24 hours after CD3ε and CD28 ligation, both CD4^{+} and CD8^{+} human T cells treated with panarginase inhibitors presented higher frequencies of CD69^{+} cells and CD62L^{lo} cells (Supplemental Figure 3, C–F). In parallel, ELISA and in vitro restimulation experiments revealed that activated *Arg2*$^{-/-}$ cells produce higher amounts of IFN-γ (Figure 3, D and E). Additionally, qPCR analysis demonstrated that activated *Arg2*$^{-/-}$ cells exhibited stronger induction of *Ifng* and *Il2* mRNAs (Figure 3, F and G), while the induction of mRNAs encoding key enzymes involved in nitric oxide production (*Nos2*) and glucose metabolism (*Gapdh*) remained unaffected (Figure 3, H and I).

To obtain a more in-depth description of the altered properties of *Arg2*$^{-/-}$ CD8^{+} T cells, we performed a time-course transcriptome analysis by RNA sequencing (RNA-seq) of in vitro–activated WT and *Arg2*$^{-/-}$ OT-I cells. An unbiased strategy based on a comprehensive gene set enrichment analysis (GSEA) was used to identify key pathways that are differentially regulated in *Arg2*$^{-/-}$ T cells (Figure 4A and Supplemental Figure 4). Several functions were significantly upregulated at most time points in *Arg2*$^{-/-}$ cells relative to WT cells, including "cytotoxicity," "IFN-γ signalling," "cytokines and inflammatory response," and "IL-2 signalling" categories (Figure 4A and Supplemental Figure 4). Other functions, such as "biosynthesis of amino acids," were downregulated at early time points but equalized at later time points. Many key genes within the upregulated categories were expressed more strongly in *Arg2*$^{-/-}$ cells after 2, 6, and 12 hours of activation, although some were already elevated prior to activation (0 hours), suggesting that *Arg2*$^{-/-}$ cells could be primed to respond more strongly (Figure 4, B–F).

Notable cytotoxicity genes upregulated in *Arg2*$^{-/-}$ cells were those encoding granzymes, perforin, and Fas ligand. Key cytokine and cytokine receptor genes upregulated in *Arg2*$^{-/-}$ cells included those for IFN-γ (*Ifng*) and one of its receptor subunits (*Ifngr1*), IL-2 (*Il2*) and its 3 receptor subunits (*Il2ra, Il2rb, Il2rg*), GM-CSF (*Csf2*), IL-3 (*Il3*), and TNF-α (*Tnf*). Three genes (*Eomes*, *Tbx21*, *Runx2*) encoding transcription factors implicated in T cell differentiation were upregulated in *Arg2*$^{-/-}$ cells. Finally, genes encoding various cell surface proteins, including the activation marker CD69 (*Cd69*), were upregulated in *Arg2*$^{-/-}$ cells. Conversely, the genes encoding 2 negative costimulatory receptors, CTLA-4 (*Ctla4*) and PD-1 (*Pdcd1*), were downregulated in *Arg2*$^{-/-}$ cells.

A similar overall picture was obtained by means of a proteomic analysis performed 72 hours after activation (Figure 4G). Proteins upregulated in the *Arg2*$^{-/-}$ cells versus WT cells included the transcription factors T-bet, Eomes, Runx2, and molecules exerting key CD8^{+} T cell effector functions (granzymes, perforin, IFN-γ, TNF-α), whereas inhibitory receptors were downregulated (CTLA-4, PD-1, Lag3). These results indicate that activated *Arg2*$^{-/-}$ CD8^{+} T cells acquire a more robust effector phenotype than their WT counterparts and are likely to be less sensitive to negative checkpoint stimuli.

Improved antitumor response by adoptively transferred CD8^{+} T cells lacking Arg2. To assess the impact of a T cell–specific deletion of Arg2 on tumor control in vivo, we next performed adoptive transfer experiments in which OT-I or *Arg2*$^{-/-}$ OT-I T cells were transferred into MC38-OVA tumor-bearing WT hosts, which were then immunized 1 day later with OVA$_{257-264}$ and CpG-B. As T cell donors, we used mixed BM chimeras generated by reconstituting irradiated WT recipients with a 9:1 mixture of *Rag2*$^{-/-}$ BM and either OT-I or *Arg2*$^{-/-}$ OT-I BM (Figure 5A). This strategy was used to ensure that results could be attributed to a T cell–intrinsic deficiency of Arg2 rather than to potential confounding effects resulting from development of the T cells in a full *Arg2*-deficient background. The CD45.1 marker was used to verify reconstitution in the mixed BM chimeras (Supplemental Figure 5, A–F). The transferred *Arg2*$^{-/-}$ OT-I cells were markedly superior at reducing tumor growth relative to Arg2-proficient OT-I cells (Figure 5B), thereby leading to prolonged mouse survival (Figure 5C). *Arg2*$^{-/-}$ OT-I cells actually induced the complete elimination of tumors in a greater proportion of mice; after 40 days, 44% (7 of 16) of mice having received *Arg2*$^{-/-}$ OT-I cells were tumor free, compared with only 12% in mice having received OT-I cells (Figure 5D). Importantly, using OT-I cells derived from mixed BM chimeras (Figure 5, A–D) yielded results comparable with those obtained using OT-I cells isolated directly from germline *Arg2*$^{-/-}$ OT-I and OT-I mice (Figure 5E), indicating that the enhanced antitumor function of *Arg2*$^{-/-}$ OT-I T cells is indeed

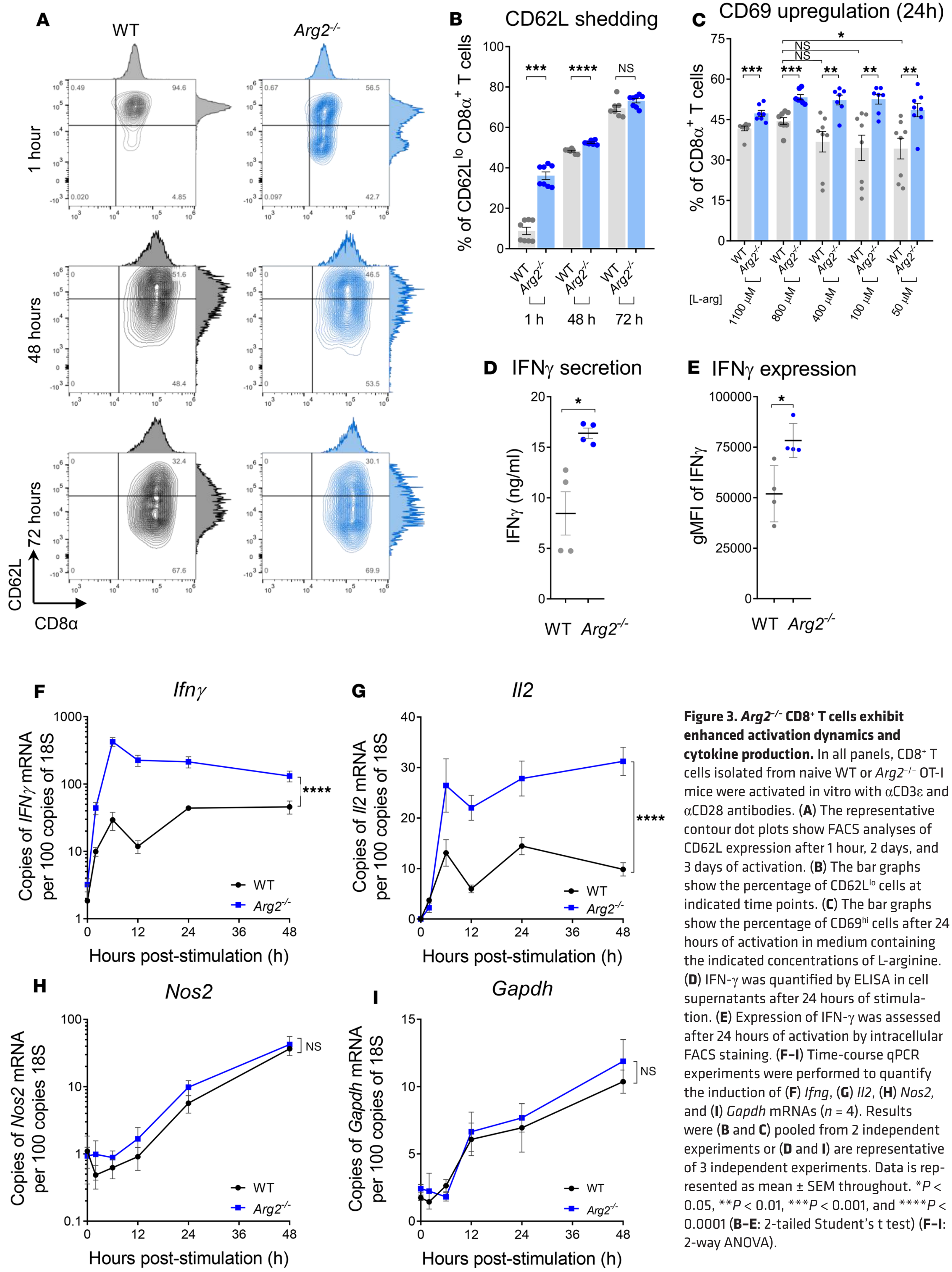

Figure 3. *Arg2*$^{-/-}$ CD8^{+} T cells exhibit enhanced activation dynamics and cytokine production. In all panels, CD8^{+} T cells isolated from naive WT or *Arg2*$^{-/-}$ OT-I mice were activated in vitro with αCD3ε and αCD28 antibodies. (**A**) The representative contour dot plots show FACS analyses of CD62L expression after 1 hour, 2 days, and 3 days of activation. (**B**) The bar graphs show the percentage of CD62L^{lo} cells at indicated time points. (**C**) The bar graphs show the percentage of CD69^{hi} cells after 24 hours of activation in medium containing the indicated concentrations of L-arginine. (**D**) IFN-γ was quantified by ELISA in cell supernatants after 24 hours of stimulation. (**E**) Expression of IFN-γ was assessed after 24 hours of activation by intracellular FACS staining. (**F–I**) Time-course qPCR experiments were performed to quantify the induction of (**F**) *Ifng*, (**G**) *Il2*, (**H**) *Nos2*, and (**I**) *Gapdh* mRNAs ($n = 4$). Results were (**B and C**) pooled from 2 independent experiments or (**D and I**) are representative of 3 independent experiments. Data is represented as mean ± SEM throughout. $^{*}P < 0.05$, $^{**}P < 0.01$, $^{***}P < 0.001$, and $^{****}P < 0.0001$ (**B–E**: 2-tailed Student's t test) (**F–I**: 2-way ANOVA).

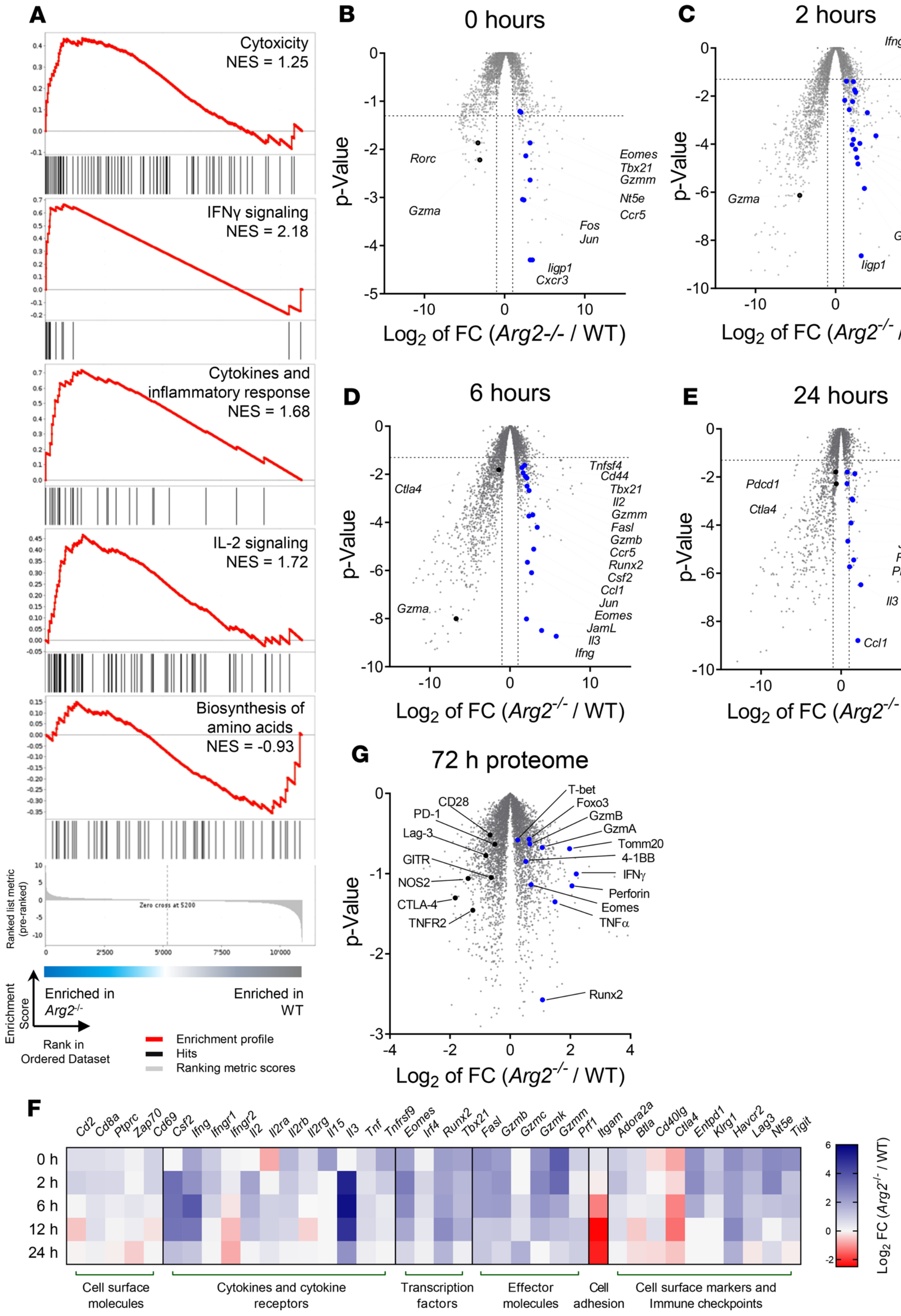

Figure 4. Activated *Arg2*$^{-/-}$ CD8$^+$ T cells exhibit faster and stronger upregulation of key genes implicated in CD8$^+$ T cell function. WT or *Arg2*$^{-/-}$ OT-I CD8$^+$ T cells were activated in vitro with αCD3ε and αCD28 antibodies, and their transcriptomes were characterized by RNA-seq after 0, 2, 6, 12, and 24 hours of activation. (**A**) The graphs show the results of a GSEA performed for the indicated gene sets in cells activated for 6 hours. The normalized enrichment score (NES) is indicated. (**B–E**) The volcano plots represent the comparisons between the transcriptomes of WT and *Arg2*$^{-/-}$ CD8$^+$ T cells at the indicated time points: fold-change (FC) in mRNA expression in *Arg2*$^{-/-}$ relative to WT cells is plotted as a function of the *P* value (Wald test, GLM in edgeR). Dots corresponding to mRNAs for key functionally relevant genes are indicated. (**F**) The heatmap represents the FC in mRNA expression in *Arg2*$^{-/-}$ relative to WT cells, in all time points analyzed, for selected genes grouped according to the indicated functionally relevant categories. (**G**) WT or *Arg2*$^{-/-}$ OT-I CD8$^+$ T cells were activated in vitro with αCD3ε and αCD28 antibodies, and the proteome was analyzed after 72 hours by LC-MS. The volcano plot represents comparisons between the proteomes of WT and *Arg2*$^{-/-}$ CD8$^+$ T cells: FC in protein expression in *Arg2*$^{-/-}$ relative to WT cells is plotted as a function of the *P* value (2- tailed Welch *t* test). Dots corresponding to key functionally relevant proteins are indicated. *P* values have been adjusted using the Benjamini-Hochberg procedure.

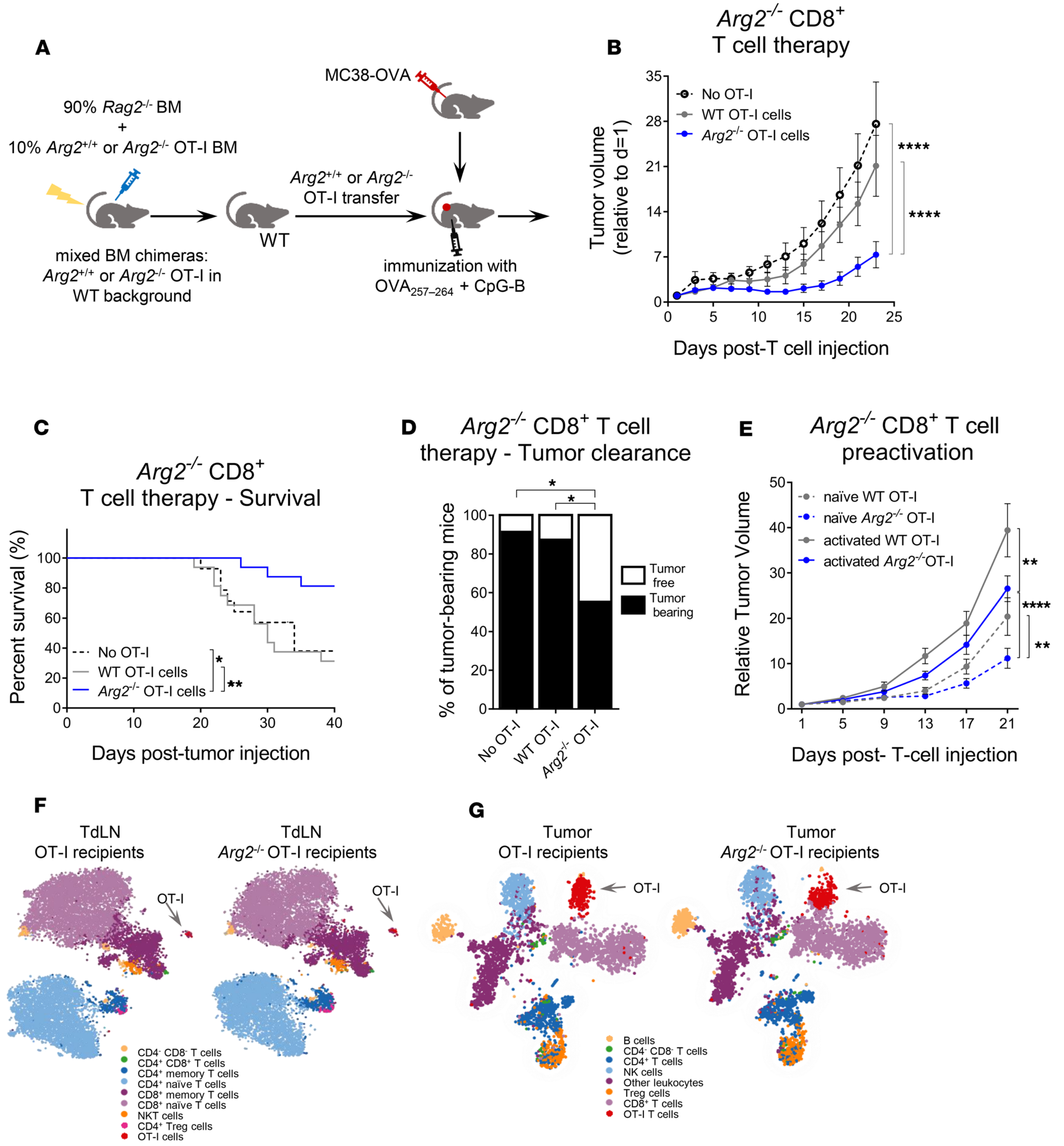

Figure 5. Endogenous *Arg2* in CD8$^+$ T cells is a cell-intrinsic regulator of their antitumor function. (**A**) The scheme illustrates the experimental setting used in panels **B–D**, **F**, and **G**. Five days prior to adoptive T cell transfer, 0.5 × 10^6 MC38-OVA cells were implanted s.c. into WT host. At day 0, 1 × 10^6 to 1.5 × 10^6 CD8$^+$ T cells isolated from naive WT or *Arg2*$^{-/-}$ mixed BM chimeric mice were adoptively transferred into the tumor-bearing mice. Control mice received no T cells. One day after T cell transfer, mice were immunized s.c. with OVA$_{257–264}$ and CpG-B. (**B**) Tumor growth, (**C**) mouse survival, and (**D**) tumor clearance rates at day 40 were assessed (n = 12–15). (**E**) Tumor growth was assessed using a setting identical to that in **A**, except that tumor-bearing mice received naive or 6-day preactivated CD8$^+$ T cells derived from WT or *Arg2*$^{-/-}$ OT-I mice (n = 11–12). Only mice transferred with naive cells were primed in vivo by s.c. immunization with CpG-B and OVA$_{257–264}$. (**F** and **G**) t-SNE plots showing the FlowSOM-guided metaclustering gated on (**F**) TCRb$^+$ T cells present in the TdLNs or gated on (**G**) CD45$^+$ cells infiltrating the tumors of WT tumor-bearing mice having received WT (left) or *Arg2*$^{-/-}$ (right) OT-I cells. (**B–E**) Results were pooled from 2 or 3 independent experiments. Data is represented as mean ± SEM throughout. *P < 0.05, **P < 0.01, and ****P < 0.0001 (**B** and **E**: 2-way ANOVA) (**C**: log-rank Mantel-Cox test) (**D**: Fisher's exact test).

cell intrinsic. Additionally, enhanced control of tumor growth by *Arg2*$^{-/-}$ OT-I cells relative to OT-I cells was evident both when transferred cells were activated in vivo by immunization and when the cells were preactivated in vitro for 6 days prior to transfer (Figure 5E). This increased tumor control by preactivated *Arg2*$^{-/-}$ OT-I cells reinforces the phenotypic data indicating that in vitro–activated *Arg2*$^{-/-}$ OT-I cells exhibit enhanced effector functions compared with OT-I cells.

To clarify the relative impacts on antitumor immune responses of the transferred OT-I and *Arg2*$^{-/-}$ OT-I cells, we performed high-dimensional flow cytometric analyses of global TdLNs and TIL populations at day 8 after OT-I transfer (Figure 5, F and G, and Supplemental Figure 6, A–D). In both TdLNs and tumors, the overall compositions of the lymphocyte populations were similar between mice having received OT-I and *Arg2*$^{-/-}$ OT-I cells. Furthermore, OT-I and *Arg2*$^{-/-}$ OT-I T cells were enriched in the tumors to similar extents relative to the TdLNs. Taken together, these results suggest that the enhanced antitumor potential of *Arg2*$^{-/-}$ OT-I cells is a cell-intrinsic property that is independent of their expansion and tumor-homing properties, or of indirect repercussions on other lymphoid cells.

To further investigate the impact of Arg2 deficiency on the spatiotemporal dynamics of tumor-specific T cell responses, equal numbers of naive OT-I and *Arg2*$^{-/-}$ OT-I CD8$^+$ T cells were cotransferred into MC38-OVA tumor-bearing mice, and their distribution in the hosts was assessed by flow cytometry in key locations and at different time points after OVA$_{257–264}$ immunization (Figure 6A). The CD45.1 marker was used to discriminate both OT-I (CD45.1$^{+/+}$) and *Arg2*$^{-/-}$ OT-I (CD45.1$^{+/-}$) cells from endogenous cells (Figure 6B). The overall dynamics were similar for OT-I and *Arg2*$^{-/-}$ OT-I cells (Figure 6, C and D). At early stages (3–4 days), both cell types were most abundant in the TdLNs and to a lesser extent in the spleen and nondraining LNs (ndLNs). They then accumulated in the blood (peaking at day 6) and infiltrated the tumors (as of day 6). The ratio between OT-I and *Arg2*$^{-/-}$ OT-I cells was close to 1:1 in the TdLNs and tumors until day 8 (Figure 6E). By day 15, however, *Arg2*$^{-/-}$ OT-I cells were markedly more frequent than OT-I cells in both the TdLNs and tumors (Figure 6E), suggesting that they mount a more persistent antitumor response than their WT counterparts.

We next assessed the relative proportions of OT-I and *Arg2*$^{-/-}$ OT-I cells present in the viable and dead cell fractions (Figure 6F) found in TdLNs or in tumors at days 3, 6, and 15. Inside the tumors, *Arg2*$^{-/-}$ OT-I cells were overrepresented in the dead cell fraction relative to the viable fraction at all 3 time points (Figure 6G). In contrast, no preferential death of *Arg2*$^{-/-}$ OT-I cells was evident in the TdLNs (Figure 6H). Enhanced accumulation of dead *Arg2*$^{-/-}$ OT-I cells in the tumors suggests that these cells are capable of mounting a more active antitumor response associated with increased activation-induced cell death at the effector site.

To confirm the alterations in functionally relevant markers observed in vitro, we next examined IFN-γ and PD-1 expression on OT-I and *Arg2*$^{-/-}$ OT-I cells in both TdLNs and tumors at day 7. Frequencies of IFN-γ$^+$ cells were greater in *Arg2*$^{-/-}$ OT-I cells in both the TdLNs and tumors (Figure 6I). Additionally, PD-1 expression was significantly lower on *Arg2*$^{-/-}$ OT-I cells in the tumors (Figure 6J). Increased IFN-γ and reduced PD-1 expression by *Arg2*$^{-/-}$ OT-I cells in the tumor was consistent with the in vitro data, and show that *Arg2*$^{-/-}$ cells develop more sustained responses, even in the context of the TME.

To further investigate the increase in T cell persistence, we next compared the memory formation and survival of OT-I and *Arg2*$^{-/-}$ OT-I cells transferred into OVA$_{257–264}$ immunized mice. Twenty-eight days after immunization, OT-I and *Arg2*$^{-/-}$ OT-I cells were found at comparable frequencies in the dLNs, ndLNs, and spleens (Figure 6K). However, the *Arg2*$^{-/-}$ cells exhibited a greater proportion of CD44^{hi}CD62L^{hi} central memory T cells (Tcm) in the dLN, but not in the ndLN or spleen (Figure 6L). Expression of the lymphoid tissue homing receptor CCR7 by *Arg2*$^{-/-}$ cells remained similar to their WT counterparts in both the LN and spleen (Figure 6M). Taken together, these results suggest that *Arg2* deficiency leads to increased development of Tcm rather than to preferential recruitment to secondary lymphoid organs.

Arg2$^{-/-}$ *CD8*$^+$ *T cells are more resistant to an arginine-poor TME*. Intratumoral arginine depletion by increased arginase activity contributes to creating an immunosuppressive TME. To determine if the intracellular deletion of Arg2 might compensate for the extracellular arginine depletion and render *Arg2*$^{-/-}$ CD8$^+$ T cells more resistant to this immunosuppressive mechanism (i.e., to an arginase-active TME), we generated MC38-OVA cells overexpressing Arg2. Strong overexpression was documented at the mRNA and protein levels (Figure 7, A and B). Control experiments demonstrated that Arg2 overexpression did not affect proliferation of the tumor cells in cell cultures (Figure 7C) or tumor growth in *Rag2*$^{-/-}$ mice, which lack an adaptive immune system (Figure 7D). In contrast, the Arg2-overexpressing tumors grew more rapidly in WT mice, confirming the immunosuppressive effect of Arg2 overexpression on the adaptive antitumor immune response (Figure 7E). We next assessed

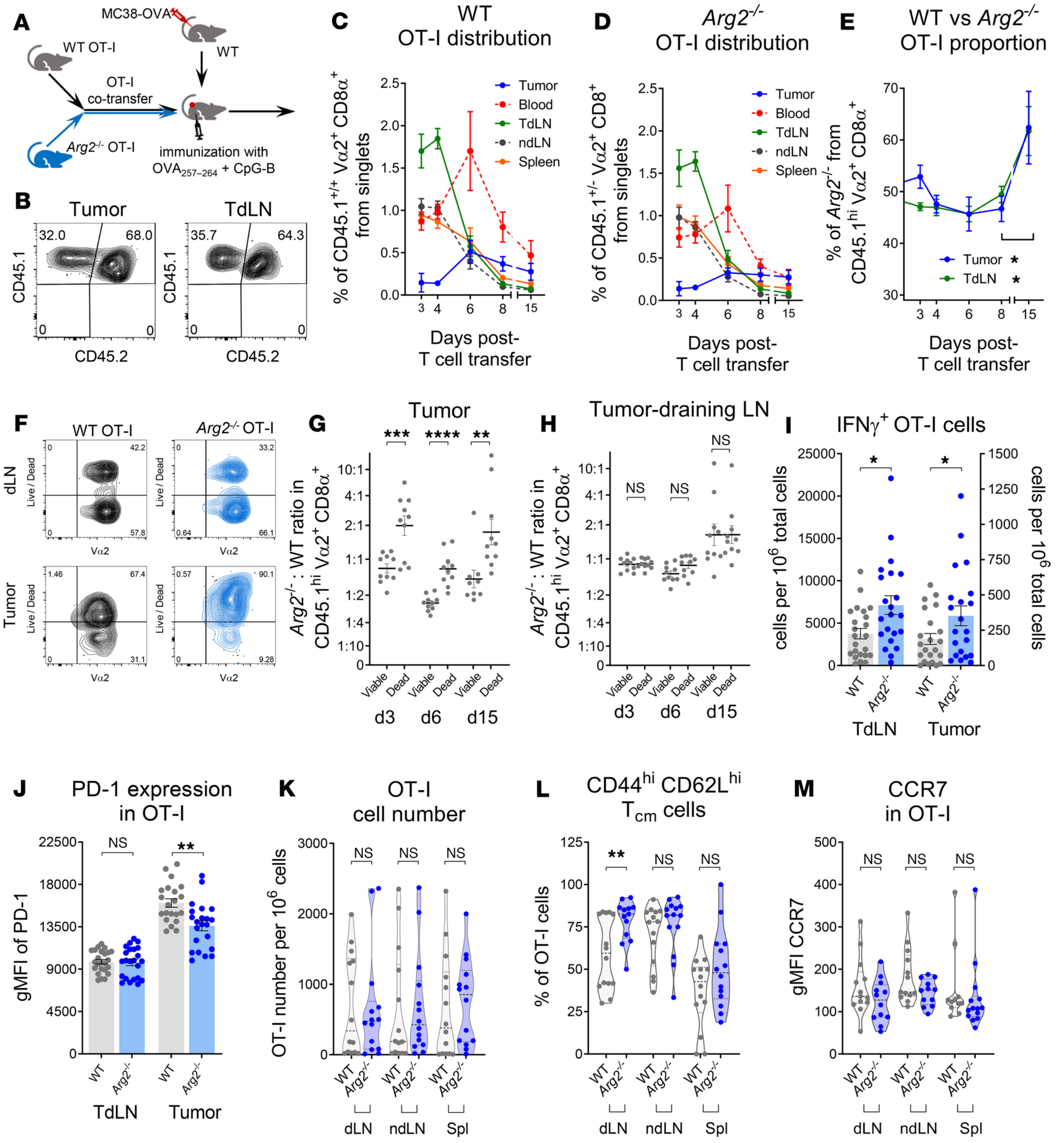

Figure 6. *Arg2* deletion enhances the persistence of antitumor CD8⁺ T cell responses and increases differentiation into Tcm cells. (**A**) The scheme illustrates the experimental setting used in panels **B–H**. The approach was similar to that in Figure 5A, except that tumor-bearing mice were adoptively transferred with a 1:1 mix of naive WT and *Arg2*$^{-/-}$ cells (1 × 10^6 to 1.3 × 10^6 total cells). (**B**) The representative contour plots illustrate the approach used in **C** and **D** to use CD45.1 staining to discriminate between WT CD45.1$^{+/+}$ and *Arg2*$^{-/-}$ CD45.1$^{+/-}$ CD8$^+$ OT-I cells. (**C** and **D**) The graphs summarize the spatiotemporal distribution of adoptively transferred WT (**C**) or *Arg2*$^{-/-}$ (**D**) CD8$^+$ OT-I cells during the course of the antitumor response (n = 10). (**E**) The graphs show the percentage of *Arg2*$^{-/-}$ cells within the total transferred OT-I cell populations found at the indicated time points in the TdLNs and tumors (n = 10). (**F**) The representative contour plots illustrate how viable and dead fractions were quantified 15 days after transfer within the cotransferred WT and *Arg2*$^{-/-}$ CD8$^+$ OT-I cell populations in the TdLNs (top) and tumor infiltrates (bottom). (**G** and **H**) The graphs summarize the *Arg2*$^{-/-}$ versus WT CD8$^+$ OT-I cell ratios found at different time points within the viable and dead cell fractions in tumors (**G**) or in TdLNs (**H**). (**I** and **J**) In the setting illustrated in Figure 5A, flow cytometry was used 8 days after transfer to quantify the frequencies of IFN-γ$^+$ cells in WT and *Arg2*$^{-/-}$ OT-I cell populations (**I**) or the expression of PD-1 by WT and *Arg2*$^{-/-}$ OT-I cells (**J**) in TdLNs and tumor infiltrates. (**K–M**) WT CD45.1$^{+/+}$ or *Arg2*$^{-/-}$ CD45.1$^{+/-}$ CD8$^+$ OT-I cells were adoptively transferred into naive WT hosts, which were immunized with CpG-B and OVA$_{257-264}$ 24 hours later. Cell frequency (**K**), central/effector memory differentiation (**L**), and CCR7 (**M**) were analyzed by flow cytometry in OT-I cells found in spleen (Spl), draining (dLN), and nondraining lymph nodes (ndLN) 28 days after immunization. Violin plots (**K**, **L**, **M**) show the median and quartiles. (**C–E** and **G–M**) Results were pooled from 2 or 3 independent experiments. *P < 0.05, **P < 0.01, and ***P < 0.001 (**G–M**: 2-tailed Student's t test) (**E**: 2-tailed Welch's t tests)

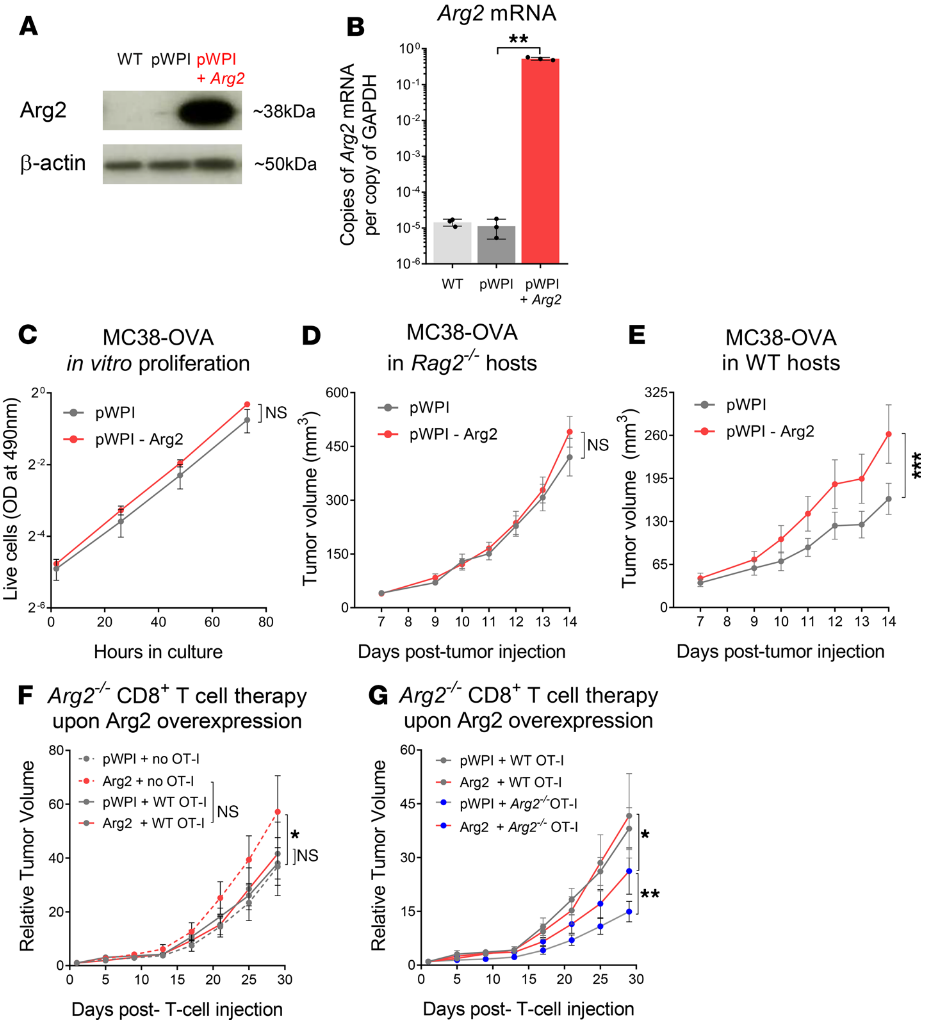

Figure 7. *Arg2$^{-/-}$* CD8$^+$ T cells are partially protected against an immunosuppressive TME induced by overexpression of arginase 2 in tumor cells. Quantification by (**A**) Western blot of Arg2 protein and (**B**) qPCR of *Arg2* mRNA abundance in control (parental or pWPI-vector transduced) and Arg2-overexpressing MC38-OVA cells. (**C**) An MTS-based assay was used to compare the in vitro proliferation of control (pWPI-transduced) and Arg2-overexpressing tumor cells ($n = 3$). (**D** and **E**) Growth of control (pWPI-transduced) and Arg2-overexpressing tumors was compared in (**D**) *Rag2$^{-/-}$* ($n = 10–11$) or (**E**) WT hosts ($n = 15–16$). (**F** and **G**) WT mice were implanted with control (pWPI-transduced) or Arg2-ovexpressing tumors; when tumors were palpable (after 5 days), WT or *Arg2$^{-/-}$* OT-I cells were adoptively transferred, and mice were immunized the next day with CpG-B and OVA$_{257–264}$ ($n = 14$). Tumor-bearing mice receiving no OT-I cells were used as controls. To improve visualization, tumor growth curves are shown separately for (**F**) groups having received no cells or WT OT-I cells and (**G**) groups having received WT or *Arg2$^{-/-}$* OT-I cells. (**B**) Results are representative of 2 independent experiments or (**C–G**) were pooled from 2 or 3 independent experiments. (**C**) Statistical analysis was performed using 2-way ANOVA. Data is represented as (**B**) mean ± SD or (**D–G**) as mean ± SEM. $^*P < 0.05$, $^{**}P < 0.01$, and $^{***}P < 0.001$ (**B**: 2-tailed Student's *t* test) (**C–G**: 2-way ANOVA).

susceptibility of the Arg2-overexpressing tumors to control by transferred OT-I and *Arg2$^{-/-}$* OT-I cells (Figure 7, F and G). The *Arg2$^{-/-}$* OT-I cells were more efficient than OT-I cells at inhibiting the growth of both control and Arg2-overexpressing tumors, although they were, as expected, less efficient at suppressing growth of the latter. *Arg2$^{-/-}$* OT-I cells, thus, have an advantage over OT-I cells in being able to function in an immunosuppressive TME exhibiting reduced arginine availability.

CD8$^+$ T cell–intrinsic Arg2 deficiency synergizes with PD-1 blockade. Tumors can induce exhaustion of tumor-infiltrating T cells both by subverting the coinhibitory PD-1/PD-L1 checkpoint axis (18) and by establishing competition for essential molecular nutrients, including arginine (19). Given that *Arg2$^{-/-}$* T cells exhibit an enhanced antitumor function, even slightly superior in an arginine-poor microenvironment (Figure 3C, and Figure 7, F and G), we assessed whether this feature might be potentialized by PD-1 blockade.

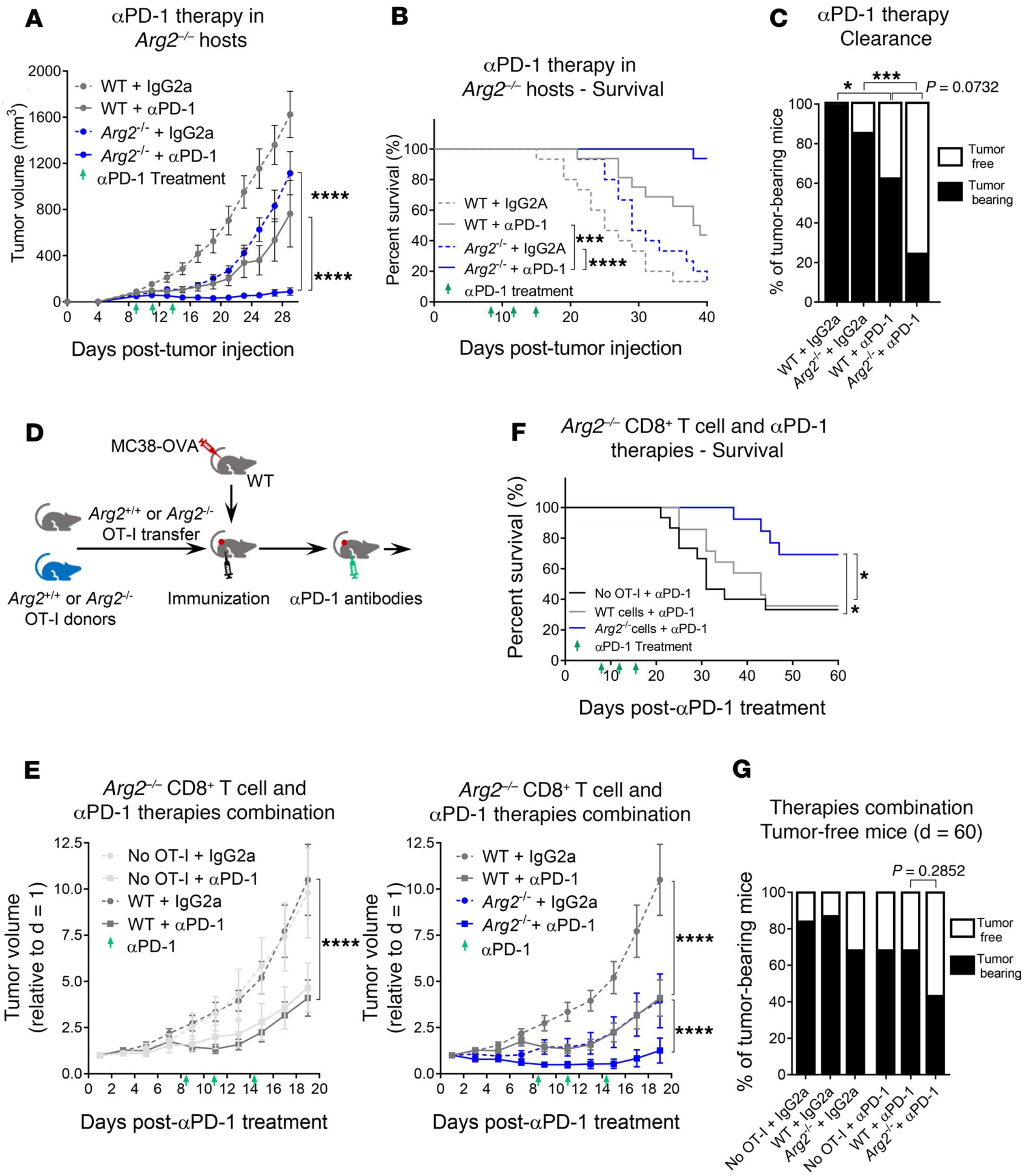

Figure 8. Tumor growth is inhibited synergistically by PD-1 blockade and either germline or CD8⁺ T cell–intrinsic deletion of *Arg2*. (**A**–**C**) MC38-OVA cells were implanted s.c. into WT or *Arg2*$^{-/-}$ hosts, which were then treated with 200 μg i.p. injections of isotype control (IgG2a) or anti–PD-1 antibodies after 8, 11, and 14 days (green arrows). The results show (**A**) tumor growth, (**B**) mouse survival, and (**C**) tumor clearance rates at day 40 after tumor injection (n = 14–16). (**D**) The scheme illustrates the experimental setting used in panels **E** and **F**. WT mice were implanted with MC38-OVA cells; when tumors were palpable (after 5 days), WT or *Arg2*$^{-/-}$ OT-I cells were adoptively transferred, and mice were immunized the following day with OVA$_{257-264}$ and CpG-B. Finally, the mice were treated with 200 μg i.p. injections of isotype control (IgG2a) or anti–PD-1 antibodies at days 8, 11, and 14 after T cell transfer (green arrows). Mice receiving no OT-I cells were used as controls. The results show (**E**) tumor growth, (**F**) mouse survival, and (**G**) tumor clearance rates at day 60 after tumor injection (n = 14–16). Isotype control data not shown in **F**, and in **E**, data were split into 2 graphs for clarity. (**A**–**F**) Results were pooled from 2 independent experiments. (**A** and **E**) Statistical analysis was performed using 2-way ANOVA. (**A** and **E**) Data is represented as mean ± SEM. *$P < 0.05$, ***$P < 0.001$, and ****$P < 0.0001$ (**A** and **E**: 2-way ANOVA) (**B** and **F**: log-rank Mantel-Cox test) (**C** and **G**: Fisher's exact test).

In a first approach, WT and *Arg2*$^{-/-}$ mice bearing MC38-OVA tumors were treated with isotype control or blocking anti–PD-1 antibodies. Compared with the individual impacts observed for *Arg2* deficiency or PD-1 blockade alone, PD-1 blockade in *Arg2*$^{-/-}$ mice led to a dramatic reduction in tumor growth, markedly prolonged mouse survival, and an increased rate of tumor clearance, with 75% tumor-free individuals in anti–PD-1–treated *Arg2*$^{-/-}$ mice versus 37% for PD-1 blockade alone (P = 0.732) and 14% for Arg2 deficiency alone

($P < 0.001$) (Figure 8, A–C). In a second approach, we explored the benefit of combining adoptive *Arg2*$^{-/-}$ OT-I transfer and PD-1 blockade in WT tumor-bearing mice (Figure 8D). In this setting, we again observed synergy between the T cell–intrinsic Arg2 deficiency and PD-1 blockade. Compared with mice that had received only *Arg2*$^{-/-}$ OT-I cells or anti–PD-1 antibodies, those that were submitted to the combined treatment exhibited a stronger reduction in tumor growth, prolonged survival, and increased tumor clearance rates (Figure 8, E–G).

Discussion

Studies on the role of L-arginine metabolism in immune responses have focused almost exclusively on the requirement of sufficient extracellular arginine availability for effective T cell activation and on the immunosuppressive effect of Arg1-mediated arginine depletion, particularly for immunosuppression of antitumor T cell responses in the TME. In contrast, the roles of Arg2-mediated arginine metabolism in immune responses have remained largely unexplored. We show here — using in vivo murine tumor models, T cell transfer approaches, flow cytometry, proteomics, and transcriptomics — that genetic ablation of Arg2 expression in CD8$^+$ T cells strengthens, in a cell-autonomous manner, their effector functions and their ability to mount more robust and persistent antitumor responses.

In agreement with the enhanced antitumor function of Arg2-deficient CD8$^+$ T cells, CD8$^+$ T cell–depletion experiments demonstrated that impaired tumor growth in Arg2-deficient mice could be attributed largely to increased antitumor CD8$^+$ T cell responses. Interestingly, however, depletion of CD4$^+$ T cells selectively improved tumor control in Arg2-deficent mice, indicating an enhanced regulatory activity exerted by CD4$^+$ T cells in these mice. Remarkably, we also observed altered functional properties of in vitro–activated *Arg2*$^{-/-}$ OT-II cells (data not shown), suggesting that Arg2 deficiency affects the function of both CD4$^+$ and CD8$^+$ T cells. Furthermore, we have previously shown that Arg2 also regulates the function of DCs (13). It is, therefore, unlikely that the phenotype observed in germline *Arg2*$^{-/-}$ mice can be attributed entirely to altered CD8$^+$ T cell responses.

Most investigations of the influence of arginine metabolism on T cells were based on interventions affecting extracellular arginine concentrations. However, extracellular and intracellular arginine pools are not freely interchangeable (20), which implies that the extracellular arginine supply may not serve as a reliable proxy for intracellular arginine availability. We demonstrate here that disrupting intracellular hydrolysis of arginine in CD8$^+$ T cells improves their activation and effector functions; in vitro–activated *Arg2*$^{-/-}$ T cells displayed more rapid and robust activation, based on CD62L shedding and CD69 upregulation, and enhanced effector functions, including increased perforin, granzyme, FasL, and cytokine (IFN-γ and IL-2) expression. These enhanced properties of Arg2-deficient T cells were found to be independent of extracellular arginine concentrations in vitro, emphasizing the critical importance of intracellular arginine pools relative to the extracellular arginine supply.

Adoptively transferred *Arg2*$^{-/-}$ OT-I CD8$^+$ T cells were more effective than OT-I CD8$^+$ T cells at controlling tumor growth in vivo, even when tumors strongly overexpressed Arg2. The disruption of intracellular arginine catabolism, thus, partially protects tumor-infiltrating T cells against the immunosuppressive effect of arginine depletion in the TME. Taken together, these observations indicate that the intracellular homeostasis of arginine plays a pivotal role for the antitumor fitness of CD8$^+$ cytotoxic T lymphocytes (CTLs) and that the intracellular arginine pool is even more critical than the extracellular arginine supply for controlling CD8$^+$ T cell responses in vivo.

Previous studies have found increased intracellular arginine levels in activated *Arg2*$^{-/-}$ T cells, indicative of enzymatic activity in these cells (16). Furthermore, as observed for *Arg2*$^{-/-}$ mouse T cells, we found that ex vivo treatment of human PBMC–derived T cells with arginase inhibitors led to an increased activation phenotype, very similar to that observed for mouse Arg2-deficient T cells. It is, therefore, possible that the elevated intracellular arginine pool, which results from the loss of Arg2 activity, is responsible for the potentiated functional properties of *Arg2*$^{-/-}$ T cells and inhibitor-treated human T cells.

Although murine *Arg2*$^{-/-}$ CD8$^+$ T cells exhibited accelerated and more robust activation kinetics in vitro, their proliferative capacity was not altered. Furthermore, the early spatiotemporal patterns of WT and *Arg2*$^{-/-}$ CD8$^+$ T cell responses were very similar in vivo. In particular, no preferential amplification of *Arg2*$^{-/-}$ CD8$^+$ T cells was evident in vivo; at the peak of the antitumor response, WT and *Arg2*$^{-/-}$ CD8$^+$ T cells were present in equivalent numbers in both the TdLNs and tumors. Therefore, the T cell–intrinsic Arg2 deficiency does not seem to affect the priming or amplification phases of CD8$^+$ T cell responses. Instead, several lines of evidence point to a more robust and persistent effector response. First, *Arg2*$^{-/-}$ CD8$^+$ T cells acquire a more robust effector phenotype, both in vitro and in vivo. Second, both in vitro–activated and tumor-infiltrating *Arg2*$^{-/-}$ CD8$^+$ T cells exhibit lower expression of inhibitory checkpoint regulators, suggesting that *Arg2*$^{-/-}$ T cells become less exhausted or are less susceptible to immunologic inhibition. Third, tumor-infiltrating *Arg2*$^{-/-}$ CD8$^+$ T cells die preferentially in the tumor compared with WT CD8$^+$ T cells, which, in combination with the increased cytotoxic activity described in *Arg2*$^{-/-}$ hosts, suggests that they mount a more effective antitumor CTL response, leading to activation-induced cell death. Fourth, following the adoptive transfer of equal numbers of in vitro–activated WT and *Arg2*$^{-/-}$ CD8$^+$ T cells, the latter showed a superior ability to mount effective antitumor responses. Fifth,at later stages of the antitumor response, *Arg2*$^{-/-}$ CD8$^+$ T cells became dominant over cotransferred WT CD8$^+$ T cells in both the TdLNs and tumors, suggesting that Arg2-deficient cells mount more sustained antitumor responses. Finally, although it remains a subject for future studies, Arg2 deficiency in CD8$^+$ T cells enhanced the formation of long-lived CD8$^+$ Tcm, suggesting that the more robust and durable response mounted by Arg2-deficient CD8$^+$ T cells could be due to enhanced memory formation, as a more sustained source of effector cells.

Immune checkpoint (PD-1, CTLA-4) blockade has become the benchmark treatment for cancer therapy (21). We observed strong synergy between the inhibition of tumor growth induced by systemic Arg2 deficiency and anti–PD-1 therapy. We therefore hypothesize that reduced PD-1 expression by *Arg2*$^{-/-}$ T cells might render them less sensitive to inhibition by PD-L1/2 in the TME and allow them to be more readily revigorated by PD-1 blockade. Interestingly, a very similar synergistic inhibition of tumor growth was observed when PD-1 blockade was combined with the systemic administration of an arginase inhibitor (22). Promising results were also obtained by combining dietary arginine supplementation with PD-L1 blockade (23). Moreover, a strong synergistic inhibition of tumor growth was observed when we combined PD-1 blockade with the adoptive transfer of tumor-specific *Arg2*$^{-/-}$ CD8$^+$ T cells. Taken together, these results imply that arginine metabolism in T cells and the PD-1/PD-L1 axis control antitumor T cell responses via nonredundant mechanisms, thereby providing a strong rationale for combining immunotherapies based on immune checkpoint blockade with the selective targeting of Arg2 in T cells.

Our study highlights a critical T cell–intrinsic role of Arg2 in modulating the efficacy of immune responses, especially CD8$^+$ T cell–mediated antitumor responses, and has major implications for the field of cancer therapy. The previously unanticipated beneficial impact of blocking detrimental arginase activity in T cells could warrant the reassessment or redirection of therapeutic strategies based on the systemic administration of arginase inhibitors. Selective interference with Arg2 expression or activity in T cells could also form the basis for novel therapeutic modalities aimed at improving existing cancer immunotherapies, particularly CAR T cell and TIL transfer therapies. In particular, the abrogation of Arg2-mediated arginine catabolism could favor the persistence of T cell responses in such therapies.

Human tumors often upregulate arginase activity to suppress immune control via arginine depletion in the TME. In mouse models, Arg2-overexpressing tumors were also found to grow more aggressively because they inhibited adaptive immune responses. Our observation that Arg2-deficient CD8$^+$ T cells exhibit an enhanced resistance to the immunosuppressive effect of reduced extracellular arginine availability finally suggests that interfering with arginine metabolism in T cells could be particularly relevant for improving the treatment of highly immunosuppressive arginase-rich solid tumors.

Methods

Animal experimentation. Age- and sex-matched C57BL/6 mice were purchased from Charles River Laboratories. *Arg2*$^{-/-}$, *miR155*$^{-/-}$, and *Rag2*$^{-/-}$ mice were purchased from The Jackson Laboratory (020286, 007745, and 008449, respectively) and bred at Charles River Laboratory. Transgenic OT-I (OT-I^{tg}) CD45.1$^{+/+}$ mice were provided by Doron Merkler (University of Geneva) and were bred and crossed with *Arg2*$^{-/-}$ mice in our facility (University of Geneva). *β2m*$^{-/-}$ mice (002087, The Jackson Laboratory) were provided by Greta Guarda (Università della Svizzera italiana). Unless stated otherwise, mice were bred under specific pathogen-free conditions and acclimatized for more than 1 week prior to experiments.

Mouse genotyping and immunophenotyping. PCR amplification of relevant loci was performed using the primers listed in Supplemental Table 2. CD45.1 and CD45.2 typing was done by flow cytometry (clones A20 and 104; BioLegend), and presence of the OT-I transgene was assessed using anti-Vα2 and anti-Vβ5 antibodies (clones B20.1 and MR9-4; BioLegend).

Mouse histopathological analyses. Necropsies and histological evaluation were performed according to standard procedures by a board-certified veterinary pathologist. Organ weights were taken using a precision scale to the nearest thousandth of a gram (Mettler Toledo ME 802). Organ samples for histology were fixed in 4% paraformaldehyde for 24 hours. Head, spinal cord, sternum, femur, and knee joint samples were decalcified for 6–12 hours. For histology, all organs were routinely processed, embedded in paraffin, cut at 3-μm thickness, and stained with H&E. The histopathologic examination was performed in a blinded fashion by a European board-certified veterinary pathologist.

Cell lines. B16-OVA and MC38-OVA cells were maintained in RPMI-1640-Glutamax medium supplemented with 10% FBS, 50 U/mL penicillin, 50 μg/mL streptomycin, 1 mM sodium pyruvate, and 50 μM β-mercaptoethanol and under geneticin selection (0.4 mg/mL G418). All reagents were purchased from Thermo Fisher Scientific. B16-OVA and MC38-OVA were provided by Stéphanie Hugues (University of Geneva) and Pedro Romero (University of Lausanne), respectively.

Mouse tumor models. In all tumor experiments, 0.5×10^6 B16-OVA or MC38-OVA cells resuspended in PBS were injected s.c. into the back of host mice. Unless stated otherwise, 6- to 12-week-old female mice were used for experiments, and tumors were allowed to grow for different periods of time according to specific experimental designs. Tumor size was quantified using a caliper, and tumor volume was calculated using a rational ellipse formula ($\alpha^2 \times \beta \times \pi/6$, where α is the shorter axis and β is the longer axis). Excised tumors were weighed postmortem. For flow cytometry analyses, tumors were minced and processed through a 70-μm nylon mesh and digested with Collagenase D and DNAse I (Roche) in HBSS (Thermo Fisher Scientific) for 40 minutes at 37°C. TdLNs were processed through a 70-μm nylon mesh. In survival experiments, mice were withdrawn from the study after tumors had reached a volume greater than 1,200 mm^3.

Arg2 overexpression in tumor cells. *Arg2* cDNA was PCR amplified and cloned into the bicistronic lentiviral pWPI vector, which contains a GFP expression cassette for assessing transduction efficiency (13). Lentiviral particles were generated in HEK293T cells, and tumor cells were subsequently transduced (13, 19) and FACS sorted on the basis of GFP expression using a FACS AriaII (Becton Dickinson). Arg2 overexpression was assessed by Western blotting and by real-time PCR, as described below. Protein extracts were fractionated by SDS-PAGE, and Western blotting was performed using anti–mouse Arg2 (sc-20151; Santa Cruz Biotechnology) and anti–β-actin (sc-47778; Santa Cruz Biotechnology). Tumor cell in vitro proliferation assays were performed using CellTiter 96 A_{Queous} One Solution (Promega) according to manufacturer's instructions.

BM chimeras. One day prior to reconstitution, recipient mice were irradiated with 2 consecutive sublethal doses of 500 cGy. BM was extracted from the tibiae and femurs of donor mice by flushing with PBS-EDTA 0.2 mM and then gently dissociated through a 70-μm nylon mesh. For BM chimeric mice 5×10^6 to 10×10^6 cells were injected i.v. into recipient mice. For mixed BM chimeric mice, *Rag2*$^{-/-}$ BM cells were mixed at 9:1 ratio with BM cells from either OT-I^{tg} CD45.1$^{+/+}$ or *Arg2*$^{-/-}$ OT-I^{tg} CD45.1$^{+/-}$ mice, and a total of 5×10^6 to 10×10^6 cells were injected i.v. into WT recipient mice. The extent of reconstitution was assessed by flow cytometric analysis of blood cells after at least 8 weeks after BM transfer.

T cell isolation. Total CD8$^+$ or CD4$^+$ T cells from splenic and LN single cell suspensions were purified using a CD8a$^+$ or CD4$^+$ T Cell Isolation Kit (Miltenyi Biotec) and subsequently separated by AutoMACS or LS Columns (Miltenyi Biotec). Cell purity (95%) was confirmed by flow cytometry. Human PBMCs were isolated from buffy coats using Ficoll-Paque gradients, and total T cells were enriched using EasySep Human T Cell Isolation Kit (Stemcell Technologies).

In vivo killing assays. In assays with preimmunized mice, WT and *Arg2*$^{-/-}$ mice were immunized by i.p. injection of 100 μg of endotoxin-free OVA protein (Hyglos) and 50 μg of CpG-B ODN 1826 (Eurogentec) per mouse. Six days later, target splenocytes were harvested from naive WT mice, loaded or not with OVA$_{257-264}$ peptide (Invivogen), and labeled with either 2.50 μM (peptide-loaded cells) or 0.25 μM (unloaded cells) of CTV (Molecular Probes). Cells were then counted and mixed at 1:1 ratio in PBS, and 2×10^6 to 5×10^6 total target splenocytes were i.v. injected into preimmunized and naive mice. Twenty-four hours later, spleens were harvested, and splenocyte suspensions were analyzed by flow cytometry. Percentages of specific in vivo killing were calculated as (1 – [% CTV^{lo} naive/% CTV^{hi} naive]/[% CTV^{lo} immunized/% CTV^{hi} immunized]) × 100.

In assays with tumor-bearing mice, WT and *Arg2*$^{-/-}$ mice were implanted with tumors cells as described above. After 11 days, each tumor-bearing mouse received 2.4×10^6 to 6.0×10^6 total target splenocytes labeled as above with CTV. Twenty-four hours later, ipsilateral TdLNs and contralateral ndLNs were harvested, and single cell suspensions were analyzed by flow cytometry. The in vivo killing ratio was calculated as (% CTV^{lo} TdLN/% CTV^{hi} TdLN)/(% CTV^{lo} ndLN/CTV^{hi} ndLN).

For NK cell cytotoxicity assays, WT and *Arg2*$^{-/-}$ naive mice were i.v. injected with a 1:1 mixture of WT and *β2m*$^{-/-}$ splenocytes (4 × 10^6 total per mouse) labeled with 2.50 μM (WT) or 0.25 μM (*β2m*$^{-/-}$) CTV. Twenty-four hours later, spleens were harvested and processed through 70-μm nylon mesh, and single cell suspensions were analyzed by flow cytometry. The in vivo killing ratio was calculated as (% CTV^{lo}/% CTV^{hi}).

In vivo depletion and PD-1 blockade. In CD4$^+$ and CD8$^+$ T cell depletion experiments, mice received i.p. injections of relevant antibodies at days –3, –1, +1, +4, +8, +11, +15, and +18, relative to the day of tumor injection, at a dose of 4 mg/kg per mouse diluted in 100 μL of pH-matched PBS (according to the manufacturer's recommendations). The antibodies used were: anti–CD4 IgG2b antibody (clone GK1.5) or IgG2b isotype control antibody (clone LTF-2); and anti–CD8α IgG2a antibody (clone 53-6.72) or IgG2a isotype control antibody (clone 2A3). In PD-1 blockade experiments, tumor-bearing mice received i.p. injections of the relevant antibodies at days +8, +11, and +14 after tumor injection at a dose of 200 μg per mouse diluted in 100 μL of pH-matched PBS (according to manufacturer's recommendations). The antibodies used were: anti–PD-1 IgG2a antibody (clone RMP1-14) or IgG2a isotype control antibody (clone 2A3). All antibodies were purchased from BioXCell.

Adoptive T cell transfer in tumor-bearing mice. Five days after tumor implantation, each MC38-OVA tumor-bearing WT mouse received 1 × 10^6 to 2 × 10^6 OT-I^{tg} CD45.1$^{+/-}$ or *Arg2*$^{-/-}$ OT-I^{tg} CD45.1$^{+/-}$ CD8$^+$ T cells by i.v. injection in PBS. One day later, hosts were immunized with 15 μg OVA$_{257–264}$ peptide and 50 μg CpG-B ODN 1826 per mouse. Mice were sacrificed at the indicated time points, relevant LNs and tumors were harvested, blood samples were collected when applicable, and samples were processed as described above. In adoptive cotransfer experiments, OT-I^{tg} CD45.1$^{+/-}$ and *Arg2*$^{-/-}$ OT-I^{tg} CD45.1$^{+/-}$ were counted and mixed at 1:1 ratio, and 1 × 10^6 CD8$^+$ T cells were i.v. injected into each MC38-OVA tumor-bearing mouse. Mixed BM chimeric mice were used as donors of the OT-I^{tg} CD45.1$^{+/-}$ and *Arg2*$^{-/-}$ OT-I^{tg} CD45.1$^{+/-}$ CD8$^+$ T cells.

In vitro T cell activation. A total of 3 × 10^4 to 1 × 10^5 purified CD8$^+$ or CD4$^+$ T cells were cultured in NUNC MaxiSorp 96-well plates with RPMI 1640, GlutaMAX medium (Thermo Fisher Scientific) supplemented with 5% FBS, 50 U/mL penicillin and 50 μg/mL streptomycin, and 50 μM β-mercaptoethanol (Thermo Fisher Scientific). T cells were activated with plate-coated anti-CD3ε (2 μg/mL, clone 145-2C11, BioXCell) and soluble anti-CD28 (2 μg/mL, clone 37.51, Becton Dickinson). For cytokine analyses, T cells were restimulated for 4.5 hours in complete RPMI 1640 with PMA (50 ng/mL; MilliporeSigma) and ionomycin (1 μg/mL), and in the presence of 1 μg/mL Golgi-plug and 1 μg/mL Golgi-stop (Becton Dickinson). To generate medium with reduced concentrations of L-arginine, L-arginine and L-lysine free SILAC RPMI 1640 (Thermo Fischer Scientific) was supplemented with 0.2 mM of L-lysine (Sigma-Aldrich) and the indicated amounts of L-arginine (Sigma-Aldrich). Human cells were cultured in similar conditions as above, activated with plate-coated anti-CD3ε (2 μg/mL, clone OKT3, BioLegend) and soluble anti-CD28 (2 μg/mL, clone 28.6, eBioscience) and in the presence or not of ABH (MilliporeSigma), BEC (MilliporeSigma), CB-1158 (MedKoo), nor-NOHA (Merck-Millipore).

For the generation of preactivated OT-I T cells, purified OT-I CD8$^+$ T cells were cultured and activated as described above. At days 2 and 4, cells were split and cultured in fresh RPMI-complete in the additional presence of 250 U/mL murine IL-2 (Miltenyi Biotec). At day 6, cells were harvested and carefully counted for in vivo adoptive transfer.

RNA extraction and real-time PCR. Total RNA was extracted using peqGOLD TriFast following the manufacturer's instructions (PeqLab). Glycogen was used as carrier. RNA purity and integrity were assessed by gel electrophoresis using a Bioanalyzer (Agilent) at the Genomics Platform of the University of Geneva, and RNA was quantified using a Qubit fluorometer. For real-time PCR, RNA was quantified using a NanoDrop 2000 (Thermo Fisher Scientific). Totals of 500 ng (*miR155*$^{-/-}$ and *Arg2* overexpression experiments) or 200 ng (*Arg2*$^{-/-}$ experiments) were reverse transcribed using a SuperScript II reverse transcriptase kit (Invitrogen) with random hexamer primers (Thermo Fisher Scientific) following the manufacturer's instructions. Real-time PCR analyses were performed using iQ SYBR Green Supermix (Bio-Rad) in a CFX Connect Real-Time System (Bio-Rad). Expression levels were inferred from a standard curve generated with serial dilutions of input cDNA, and expression was normalized to 18S rRNA or *Gapdh* mRNA (Arg2-overexpression experiments). Primers are listed in Supplemental Table 2.

ELISA. Cell supernatants were collected and frozen at the indicated time points. Secreted IL-2 and IFN-γ were measured in NUNC MaxiSorp 96-well plates using Ready-Set-Go! kits (88-7024-22 and 88-7314-22, eBioscience), according to the manufacturer's instructions. Analysis was done using a kinetic microplate reader (Molecular Devices) at a 450-nm wavelength. A 4-parameter fit using a precalibrated standard curve was used for absolute quantification.

Flow cytometry. Samples of peripheral blood were collected in FACS Buffer (PBS + 0.5% BSA + 5 mM EDTA), and erythrocytes were lysed using 1-step Fix/Lyse solution (eBioscience) after antibody labeling. Viable cell discrimination was done by staining with Zombie Yellow (BioLegend) or near–infrared radiation (near-IR) fluorescence reactive dye (Molecular Probes) according to the manufacturer's protocol. For high-dimensional analysis, viable cell discrimination was done by staining with Zombie Aqua (BioLegend) according to the manufacturer's protocol. For proliferation assays, CTV staining was performed at 5 μM concentration for 15 minutes at 37°C in PBS. Prior to antibody staining, Fc receptors were blocked with anti-CD16/CD32 antibody treatment (clone 2.4G2, eBioscience) for 10 minutes at 4°C. Extracellular staining was performed in FACS buffer (PBS + 0.5% BSA + 5 mM EDTA) for 15 minutes at 4°C. For intracellular antigens, cells were fixed and permeabilized using Foxp3/Transcription Factor Staining Buffer Set (eBioscience) for 45 minutes at 4°C, and intracellular antigens were subsequently stained in permeabilization buffer for 45 minutes at 4°C. For high-dimensional FACS analysis, the labeling of the intracellular antigens was performed overnight at 4°C in permeabilization buffer. Extracellular and intracellular proteins were stained using the antibodies listed in Supplemental Table 3. Samples were analyzed on a Gallios (Beckman Coulter) or Attune NxT (Thermo Fisher Scientific) flow cytometer using appropriate filter sets and compensation controls. For high-dimensional FACS analysis, data were acquired on a FACSymphony (Becton Dickinson). Gates were assigned according to appropriate negative and fluorescence minus one (FMO) control populations.

L-Arginine mass spectrometry. Harvested tissues were snap frozen in liquid nitrogen and vacuum-dried overnight on a CentriVap (Labconco). Dry tissues were ground mechanically in liquid nitrogen, and 5 mg of fine powder was used for amino acid extraction using ethanol/water/diethylether/pyridine (15:15:5:1) and ammonium hydroxide 2.1×10^{-3} N (chemical reagents purchased from MilliporeSigma), in the presence of L-arginine-$^{13}C_6$,$^{15}N_4$ hydrochloride standard (Cambridge Isotope Laboratories). For analysis of circulating arginine levels, tail vein blood samples were collected in sterile Microtainer tubes (1.5 mL; Becton-Dickinson), and serum was collected after 40 minutes of clotting at room temperature and stored at –20°C until analysis. Subsequently, amino acids were extracted from 50 μL of serum samples as described above for tissue samples. Extracts were dried in a CentriVap and stored at –80°C until analysis. Dried extracts were resuspended in 10 μL 0.1 % formic acid, 70 μL borate buffer (200 mM boric acid pH 8.8 [with NaOH], 10mM tris [2-carboxyethyl]phosphine [TCEP], 1 mM ascorbic acid, 35.7 μM 13C15N-Valine) Boric acid, TCEP, and ascorbic acid were from MilliporeSigma; ^{13}C15N-Valine was from Cambridge Isotope Laboratories. The mixture was sonicated for 5 minutes, and 20 μL of 10 mM AQC (6-aminoquinolyl-*N*-hydroxysuccinimidyl carbamate, 2.85 mg/mL in acetonitrile; MilliporeSigma) was added. The sample was incubated for 15 minutes at 55°C with shaking (750 rpm) followed by overnight incubation at 24°C. After incubation, the sample was centrifuged (400 *g*, 10 minutes), and the supernatant transferred to a new insert. Liquid chromatography–mass spectrometry (LC-MS) was performed using an Accela HPLC system coupled to a TSQ Vantage Triple Stage Quadrupole Mass Spectrometer (Thermo Fisher Scientific). A total of 10 μL was loaded onto a NUCLEOSHELL RP 18 column (particle size, 2.7 μm; length, 100 mm; diameter, 2 mm) (MACHEREY-NAGEL) and a gradient was applied: solvent A, milliQ water + 0.1 % formic acid (MilliporeSigma); solvent B, isopropanol (MilliporeSigma) + 0.1 % formic acid, at a flow of 300 μL/min. The quantification of the metabolites was performed using multiple reaction monitoring (MRM). Area of arginine was normalized to the internal L-arginine-$^{13}C_6$,$^{15}N_4$ standard.

Proteomics. Cells were harvested, washed twice in D-PBS, and snap-frozen in liquid nitrogen. Frozen cell pellets were resuspended in a buffered solution containing 8 M urea. After reduction of disulphide bonds and alkylation, samples were sonicated using a Bioruptor and digested with LysC (Fujifilm) and trypsin (MilliporeSigma), and peptides were purified using StageTips (24). Peptides were analyzed on a QExactive HF mass spectrometer coupled to an nEASY 1200 liquid chromatography system as described previously (16, 25). MS raw files were analyzed using the MaxQuant software to identify proteins and quantify their relative abundances (label free quantitation; LFQ) (26).

Transcriptomics. Five independent biological replicates for each condition were analyzed at all time points. A total of 100 ng cDNA libraries were prepared using the Illumina TruSeq mRNA Stranded Kit (Illumina) according to the manufacturer's protocol. Libraries were sequenced using single-end reads (50 nt–long) on an Illumina HiSeq4000. Library preparation and sequencing were performed at the iGE3 Genomics Platform of the University of Geneva.

High-dimensional FACS analysis. For T-distributed stochastic neighbor embedding (t-SNE) and FlowSOM, the exported FCS files were uploaded in Cy3 software (Matlab based), and Arcsinh cofactors were applied to every channel. Samples were then uploaded into Rstudio, and t-SNE and FlowSOM script were performed as described before (27).

Proteome analysis. Data analysis and quality control were performed using the Perseus software (28) and the R statistical computing environment. Quality control parameters included the number of identified proteins and correct expression of the marker protein CD8. For statistical tests, missing values were imputed to simulate the distribution of low signal values. The empirically defined parameters were: normal distribution of 30% of the SD of measured values and a 1.8 SD downshift of the mean.

Transcriptome analysis. FastQ reads were mapped to the ENSEMBL reference genome (GRCm38.89) using STAR version 2.4.0j (29) with standard settings, except that any reads mapping to more than 1 location in the genome (ambiguous reads) were discarded (m = 1). A unique gene model was used to quantify reads per gene, in which all annotated exons of all annotated protein coding isoforms of a gene create a unique gene where the genomic regions of all exons are considered coming from the same RNA molecule and merged together. All reads overlapping the exons of each unique gene model were reported using featureCounts version 1.4.6-p1 (30). Gene expression was reported as raw counts and, in parallel, normalized as reads per kilobase of transcript, per million mapped reads (RPKM) in order to filter out genes with low expression values (1 RPKM) before calling for differentially expressed genes. Library size normalizations and differential gene expression calculations were performed using the package edgeR (31) designed for the R software (32). Only genes having a significant fold change (Benjamini-Hochberg corrected $P < 0.05$) were considered for the rest of the RNA-seq analysis. Gene Ontology (GO; http://geneontology.org) term and Kyoto Encyclopedia of Genes and Genomes (KEGG; https://www.genome.jp/kegg/) metabolic pathway enrichment was performed using homemade scripts for the R software (32).

For the GSEA, all annotated pathways for *Mus musculus* available on KEGG metabolic pathways database were used to generate gene sets, relative to GRCm38.89. Genes were ranked by their calculated fold-changes (decreasing ranking). A gene set analysis using the GSEA package Version 2.2 (33, 34) from the Broad Institute (MIT, Cambridge, Massachusetts, USA) was used to analyze the pattern of differential gene expression between the 2 groups. Gene set permutations were performed 1000 times for each analysis. The normalized enrichment score (NES) was calculated for each gene set. GSEA results with a nominal FDR lower than 0.05 and an absolute NES bigger than 1 were considered significant.

Data and software availability. Sequence data has been submitted to the GEO database under the accession number GSE139811.

Statistics. Statistical parameters including the exact value of n, the definition of center, dispersion and precision measures, and statistical significance are indicated in the figures and figure legends. P values of less than 0.05 were considered significant. Unless otherwise stated, bar plots and dot plots were judged using t tests. Normally distributed data were judged using 2-tailed unpaired Student's t tests; nonnormally distributed data were judged using Mann-Whitney U tests. Tumor growth curves were judged using 2-way ANOVA. Survival analyses were judged using log-rank (Mantel-Cox) tests. Bonferroni correction was used when multiple comparisons were performed. Tumor-clearance rate analyses were judged using Fisher's exact test. Differential gene expression was assessed by Wald test, using GLM in edgeR. Throughout the figures, asterisks denote statistical significance reported by the indicated statistic test ($^*P < 0.05$; $^{**}P < 0.01$; $^{***}P < 0.001$; $^{****}P < 0.0001$). Statistical analysis was performed in R or GraphPad PRISM software.

Study approval. Animal experimentation was reviewed and approved by the cantonal veterinary authority at the SCAV (Service de la consommation et des affaires vétérinaires) in Geneva, Switzerland, and performed according to Swiss animal protection laws. All blood donors at the Centre de Transfusion sanguine et don du sang of the Universtiy Hospital of Geneva provided and approved their informed consent to participate in the study.

Author contributions

AAML designed and performed experiments, analyzed the data, and prepared the figures. IDS and WR conceived the study and designed experiments. MC and FG genotyped mice, and MC performed and analyzed in vitro T cell experiments. JTH, HR, and RG performed, analyzed, and provided expertise for the mass spectrometry analyses. AP and KH performed the histopathological analyses. SL performed the bioinformatic analysis and provided feedback for other data analyses. NN performed and, together with BB, provided the expertise and feedback for high-dimensional FACS analysis. BB, TDS, and SH provided precious feedback. WR, together with IDS, supervised the work and obtained funding. AAML and WR wrote the manuscript.

Acknowledgments

We thank P. Romero for providing the MC38-OVA cells, as well as D. Merkler and G. Guarda for providing mice. We thank Q. Seguín Estévez, J. Dubrot Armendáriz, and C. Lippens for technical discussions and L. Ducimetière for technical assistance. We are also very grateful to the iGE3 Genomics platform of the University of Geneva for their advice and help in performing transcriptomics experiments. This work was supported by grants from the Swiss (WR and BB) and Geneva (WR) Cancer leagues, the NCCR Chemical Biology (JTH and HR), the Swiss National Science Foundation (310030_146130, 316030_150768, and 310030_170320 to BB; 310030_166371 to WR), the European Union FP7 Project ATECT (BB), and the University Research Priority Project Translational Cancer Research (BB). We thank G. Schneiter and C. Gameiro for invaluable technical assistance.

Address correspondence to: Walter Reith, Department of Pathology and Immunology, University of Geneva Medical School CMU, 1 rue Michel-Servet CH-1211 Geneva 4 Switzerland. Phone: 41.0.22.379.56.66; Email: walter.reith@unige.ch.

---

1. Rodriguez PC, Zea AH, Culotta KS, Zabaleta J, Ochoa JB, Ochoa AC. Regulation of T cell receptor CD3zeta chain expression by L-arginine. *J Biol Chem*. 2002;277(24):21123–21129.
2. Park KG, Hayes PD, Garlick PJ, Sewell H, Eremin O. Stimulation of lymphocyte natural cytotoxicity by L-arginine. *Lancet*. 1991;337(8742):645–646.
3. Barbul A, Sisto DA, Wasserkrug HL, Efron G. Arginine stimulates lymphocyte immune response in healthy human beings. *Surgery*. 1981;90(2):244–251.
4. Barbul A, et al. Intravenous hyperalimentation with high arginine levels improves wound healing and immune function. *J Surg Res*. 1985;38(4):328–334.
5. Barbul A, Wasserkrug HL, Yoshimura N, Tao R, Efron G. High arginine levels in intravenous hyperalimentation abrogate post-traumatic immune suppression. *J Surg Res*. 1984;36(6):620–624.
6. Murray PJ. Amino acid auxotrophy as a system of immunological control nodes. *Nat Immunol*. 2016;17(2):132–139.
7. Rodriguez PC, Zea AH, Culotta KS, Zabaleta J, Ochoa JB, Ochoa AC. Regulation of T cell receptor CD3zeta chain expression by L-arginine. *J Biol Chem*. 2002;277(24):21123–21129.
8. Rodriguez PC, Quiceno DG, Ochoa AC. L-arginine availability regulates T-lymphocyte cell-cycle progression. *Blood*. 2007;109(4):1568–1573.
9. Ochoa JB, Strange J, Kearney P, Gellin G, Endean E, Fitzpatrick E. Effects of L-arginine on the proliferation of T lymphocyte subpopulations. *JPEN J Parenter Enteral Nutr*. 2001;25(1):23–29.
10. Bronte V, Zanovello P. Regulation of immune responses by L-arginine metabolism. *Nat Rev Immunol*. 2005;5(8):641–654.
11. Caldwell RW, Rodriguez PC, Toque HA, Narayanan SP, Caldwell RB. Arginase: A Multifaceted Enzyme Important in Health and Disease. *Physiol Rev*. 2018;98(2):641–665.
12. Jenkinson CP, Grody WW, Cederbaum SD. Comparative properties of arginases. *Comp Biochem Physiol B, Biochem Mol Biol*. 1996;114(1):107–132.
13. Dunand-Sauthier I, et al. Repression of arginase-2 expression in dendritic cells by microRNA-155 is critical for promoting T cell proliferation. *J Immunol*. 2014;193(4):1690–1700.
14. Elahi S, Ertelt JM, Kinder JM, et al. Immunosuppressive CD71 + erythroid cells compromise neonatal host defence against infection. Nature. 2013;504(7478):158–162.
15. McGovern N, et al. Human fetal dendritic cells promote prenatal T-cell immune suppression through arginase-2. *Nature*. 2017;546(7660):662–666.
16. Geiger R, et al. L-Arginine Modulates T Cell Metabolism and Enhances Survival and Anti-tumor Activity. *Cell*. 2016;167(3):829–842.e13.
17. Shi O, Morris SM, Zoghbi H, Porter CW, O'Brien WE. Generation of a mouse model for arginase II deficiency by targeted disruption of the arginase II gene. *Mol Cell Biol*. 2001;21(3):811–813.
18. Okazaki T, Chikuma S, Iwai Y, Fagarasan S, Honjo T. A rheostat for immune responses: the unique properties of PD-1 and their advantages for clinical application. *Nat Immunol*. 2013;14(12):1212–1218.
19. Gabrilovich DI, Ostrand-Rosenberg S, Bronte V. Coordinated regulation of myeloid cells by tumours. *Nat Rev Immunol*. 2012;12(4):253–268.
20. Topal G, Topal JL, Brunet A, Walch L, Boucher JL, David-Dufilho M. Mitochondrial arginase II modulates nitric-oxide synthesis through nonfreely exchangeable L-arginine pools in human endothelial cells. *J Pharmacol Exp Ther*. 2006;318(3):1368–1374.
21. Ribas A, Wolchok JD. Cancer immunotherapy using checkpoint blockade. *Science*. 2018;359(6382):1350–1355.
22. Steggerda SM, et al. Inhibition of arginase by CB-1158 blocks myeloid cell-mediated immune suppression in the tumor microenvironment. *J Immunother Cancer*. 2017;5(1):101.
23. He X, Lin H, Yuan L, Li B. Combination therapy with L-arginine and α-PD-L1 antibody boosts immune response against

osteosarcoma in immunocompetent mice. *Cancer Biol Ther*. 2017;18(2):94–100.

24. Rappsilber J, Mann M, Ishihama Y. Protocol for micro-purification, enrichment, pre-fractionation and storage of peptides for proteomics using StageTips. *Nat Protoc*. 2007;2(8):1896–1906.
25. Scheltema RA, et al. The Q Exactive HF, a Benchtop mass spectrometer with a pre-filter, high-performance quadrupole and an ultra-high-field Orbitrap analyzer. *Mol Cell Proteomics*. 2014;13(12):3698–3708.
26. Cox J, Mann M. MaxQuant enables high peptide identification rates, individualized p.p.b.-range mass accuracies and proteome-wide protein quantification. *Nat Biotechnol*. 2008;26(12):1367–1372.
27. Brummelman J, et al. Development, application and computational analysis of high-dimensional fluorescent antibody panels for single-cell flow cytometry. *Nat Protoc*. 2019;14(7):1946–1969.
28. Tyanova S, et al. The Perseus computational platform for comprehensive analysis of (prote)omics data. *Nat Methods*. 2016;13(9):731–740.
29. Dobin A, et al. STAR: ultrafast universal RNA-seq aligner. *Bioinformatics*. 2013;29(1):15–21.
30. Quinlan AR, Hall IM. BEDTools: a flexible suite of utilities for comparing genomic features. *Bioinformatics*. 2010;26(6):841–842.
31. Robinson MD, McCarthy DJ, Smyth GK. edgeR: a Bioconductor package for differential expression analysis of digital gene expression data. *Bioinformatics*. 2010;26(1):139–140.
32. R Core Team. R: A language and environment for statistical computing. R Foundation for Statistical Computing, Vienna, Austria. http://www.R-project.org/. Accessed November 18, 2019.
33. Mootha VK, et al. PGC-1alpha-responsive genes involved in oxidative phosphorylation are coordinately downregulated in human diabetes. *Nat Genet*. 2003;34(3):267–273.
34. Subramanian A, et al. Gene set enrichment analysis: a knowledge-based approach for interpreting genome-wide expression profiles. *Proc Natl Acad Sci USA*. 2005;102(43):15545–15550.